UiT
THE ARCTIC UNIVERSITY OF NORWAY

Faculty of Science and Technology

Department of Physics and Technology

# Climatic variations and sediment provenance during the last 16 000 years in the North Hinlopen Trough, Svalbard

**Kristine Reppen Samuelsen**

*EOM-3901 Master's thesis in Energy, Climate and Environment*

*June 2019*

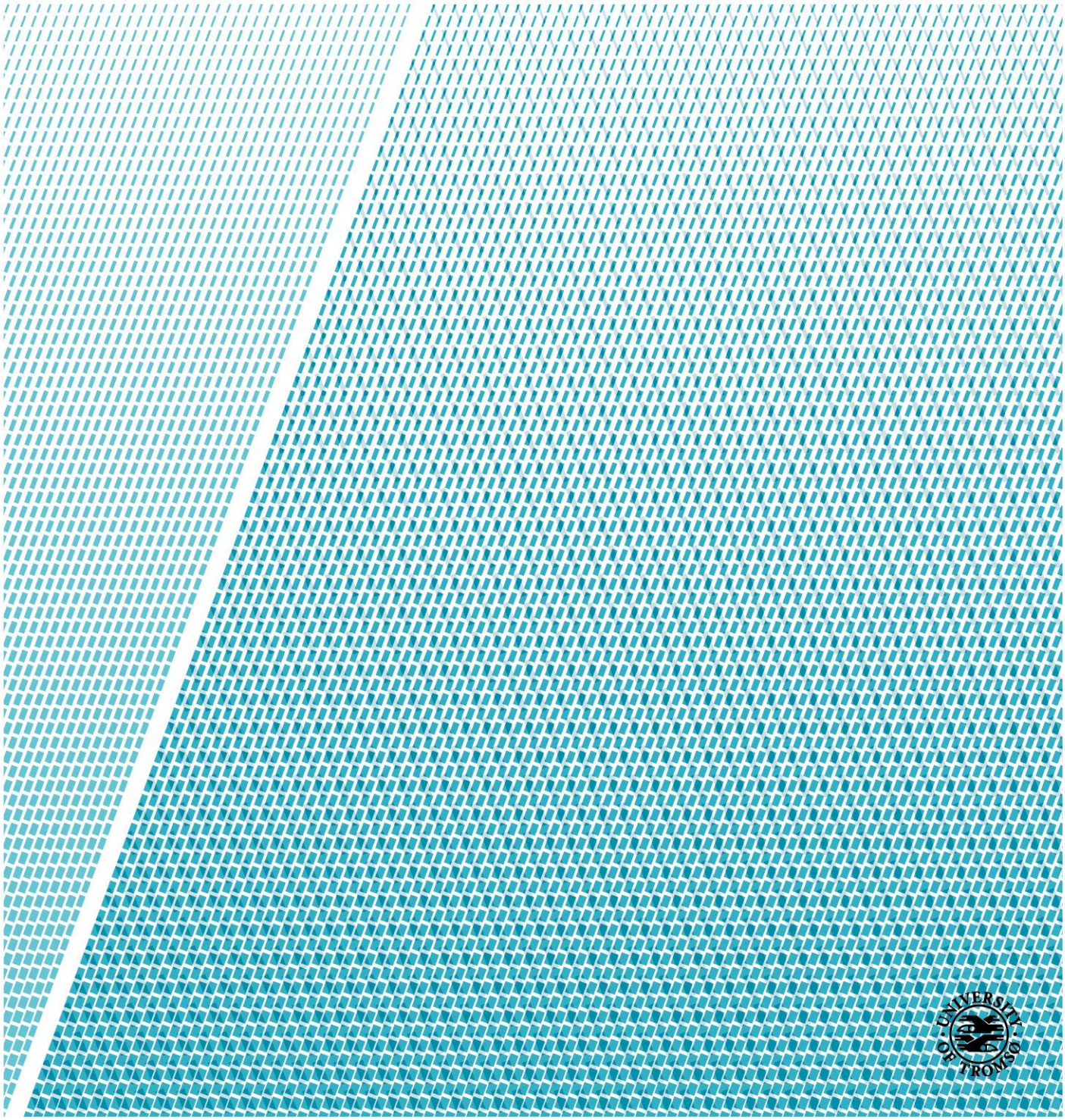

# Abstract

Gravity core HH18-1500GC retrieved from the Hinlopen Trough, Arctic Ocean, has been investigated in order to reconstruct the climatic evolution and ocean circulation over the last 16 000 years. The core was taken at the edge of the trough on the northern Svalbard shelf in order to be certain to reach into till, with the intent of dating the retreat of the ice sheet. The Fram Strait is located between Greenland and Svalbard, and is the main gateway for water and heat exchange to the Arctic Ocean. Reconstructing paleoceanography and paleoenvironmental changes in relation to climate change is important to predict future climate changes, as changes occurring in this area probably will affect the whole Arctic.

The core was divided into 5 lithological and stratigraphic units based on grain size distribution, magnetic susceptibility, ice-rafted debris data, benthic and planktonic foraminiferal analysis and content of total carbon, total organic carbon and calcium carbonate. An age model was constructed based on AMS-$^{14}$C dates and correlation with other studies. The core contains sediments from pre-Bølling (> 16 100 cal years BP), the Bølling-Allerød interstadials (16 100 – c. 13 000 cal years BP), the Younger Dryas stadial (c. 13 000 – c. 12 000 cal years BP) and the Holocene (< c. 12 000 cal years). The most recent sediments are c. 6500 cal years BP, indicating erosion or non-deposition due to strong bottom currents activity on the shelf. Five distinct pinkish layers were discovered within the Bølling-Allerød interval, correlating to increasing spectre of lightness, decreasing magnetic susceptibility and decreasing IRD content. Pink sediments were probably derived by melt water run-off from retreating glaciers, under high surface temperatures and at high sedimentation rates.

# Acknowledgement

Først og fremst ønsker jeg å takke min veileder Tine Lander Rasmussen for god veiledning og oppfølging gjennom masteroppgaven. Takk til Trine Dahl, Ingvild Hald og Karina Monsen for all hjelp på laboratoriet. Naima El Bani Altuna – thank you so much for motivating and guiding me through this paper. Your contribution is invaluable!

Fem år med studier er endelig over. Det føles godt, men samtidig litt vemodig. Jeg må takke klassekamerater på EKM for et fantastisk samhold. Det har vært mange fine stunder, som jeg aldri kommer til å glemme. Takk til geobabes på kontor 1 og 2 for alle faglige og ikke-faglige samtaler. En spesiell takk til Marie, som jeg tilbrakte utvekslingen i Southampton sammen med. Opplevelsen hadde ikke vært den samme uten deg! Kan heller ikke komme foruten Elise. Takk for at du alltid stiller opp, hva enn det måtte være.

En stor takk må rettes til familien min, som har vært støttende gjennom et krevende studieløp. Helt til slutt ønsker jeg å hedre min kjære morfar. Du vil alltid være et forbilde for meg.

Kristine Reppen Samuelsen

Tromsø, Juni 2019

# Table of contents

# 1 Introduction

The climate has been constantly changing throughout the Earth´s history, and to predict how the climate may change in the future, it is important to have knowledge about the past climate (Marshall and Plumb, 2008).

Glacials and interglacials have occurred in regular intervals of 100 000 years over the last 800 000 years (Marshall and Plumb, 2008). 90 % of the last 800 000 years, Earth has been in a glacial environment (Marshall and Plumb, 2008). Today, we are in an interglacial period. Over the past 200 years, and especially the last 50 years, the amount of carbon dioxide in the atmosphere has increased due to human activities (Houghton, 2009). Decreasing sea ice cover, increased atmospheric and oceanic temperatures, and thawing permafrost, for example, are evidence of global warming in the Arctic (Overland, 2009). Chapman and Walsh (2007) stated that most climate models indicate that the warming in the Arctic will be greater than the temperature increase at more southern latitudes.

The western and northern Svalbard margins are an interesting area of study regarding climate changes because it is where warm and cold surface water masses meet (Kristensen et al., 2013). The main gateway for water masses to the Arctic is through the Fram Strait (Saloranta and Haugan, 2001). That is why, the Fram Strait is vulnerable to climate changes, and changes occurring here may affect the whole Arctic (Serreze and Francis, 2006). In fact, the sea ice distribution and the quantity of glaciers and ice caps in the Arctic will be affected by changes in the water masses (Kristensen et al., 2013).

In this work, benthic and planktonic foraminiferal concentrations, ice-rafted debris data, magnetic susceptibility and sedimentological data will be used to reconstruct the climatic evolution and ocean circulation on the northern Svalbard margin over the last 16 000 years. This will be correlated with data from other studies for a larger regional perspective.

## 1.1 Foraminifera

Foraminifera are marine organisms widely used as microfossil proxies (Armstrong and Brasier, 2005). Javaux and Benzerara (2009) defined microfossils as “the microscopic remains of organisms”.

Foraminifera are single-celled protozoa living on the sea floor or in the water column. Foraminifera build a shell or test around their cytoplasm. These shells or tests can consist of calcium carbonate ($CaCO_3$), organic material or mineral particles (Armstrong and Brasier, 2005). When foraminifera die, they fall down to the seabed and accumulate into “carbonate ooze”. These “carbonate oozes” cover approximately half of the seabed (Kimoto, 2015). Because foraminiferal shells are easy to identify, have good preservation capability and are found world wide, they are ideal as research of climate variability. When studied, the skeletons can give information about the temperature, ocean fertility and chemostratigraphy of the ocean when the sediments were deposited (Armstrong and Brasier, 2005).

Foraminifera can be divided into benthic and planktonic foraminifera, based on their habitat (Armstrong and Brasier, 2005). There are found 6000 different species of foraminifera in the world (Jones, 1994), and only 40-50 of these species are planktonic (Schiebel and Hemleben, 2005).

Planktonic foraminifera live in the surface to sub-thermohaline layer of the ocean (Schiebel and Hemleben, 2005), to a maximum depth of about 1000 m (Kimoto, 2015). They first occurred in the mid-Jurassic, and during the mid-Cretaceous they were found all over the World´s Ocean (Schiebel and Hemleben, 2005). The different species are living in different environments, based on season, water depths, and water masses (Schiebel and Hemleben, 2005). *Neogloboquadrina pachyderma*, *Turborotalita quinqueloba* and *Globigerinita uvula* are the three most common planktonic foraminiferal species in polar oceans (Figure 1; Kimoto, 2015; Pearson et al., 2018) (Schiebel and Hemleben, 2005).

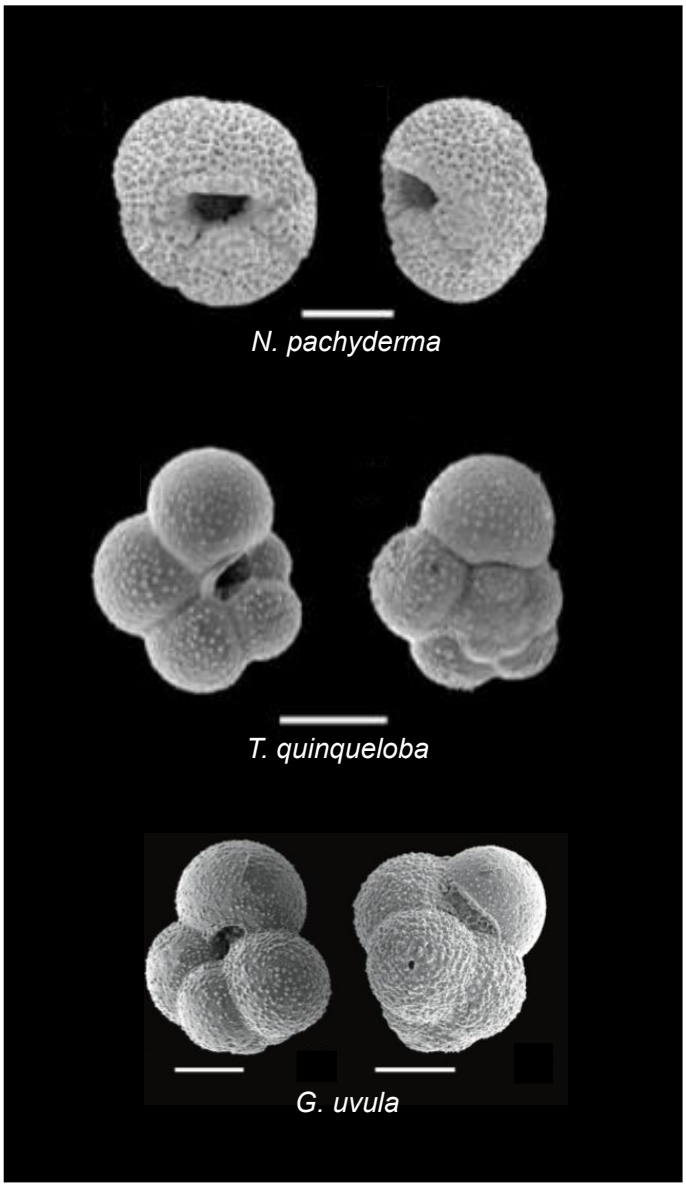


*Figure 1. Images of the most common planktonic foraminiferal species in the Arctic: Neogloboquadrina pachyderma, Turborotalita quinqueloba and Globigerinita uvula. The scanning electron microscopy (SEM) images of N. pachyderma and T. quinqueloba are taken from Kimoto (2015), while the SEM images of G. uvula are taken from Pearson et al. (2018). The white lines are scale bars, indicating 100 µm.*

Benthic foraminifera live at all depths in the ocean, and are found in most marine environments (Kimoto, 2015). Benthic foraminifera are affected by the water depth, sediment characteristics, food supply, predation and competition with other fauna (e.g. Snelgrove and Butman, 1994; Kendall, 1996). *Nonionella labradorica*, *Elphidium clavatum*, *Cassidulina neoteretis*, *Quinqueloculina arctica*, *Cibicidoides wuellerstorfi* and *Oridorsalis tener* are the most common benthic foraminiferal species in the Arctic (Figure 2; Barrientos et al., 2018).

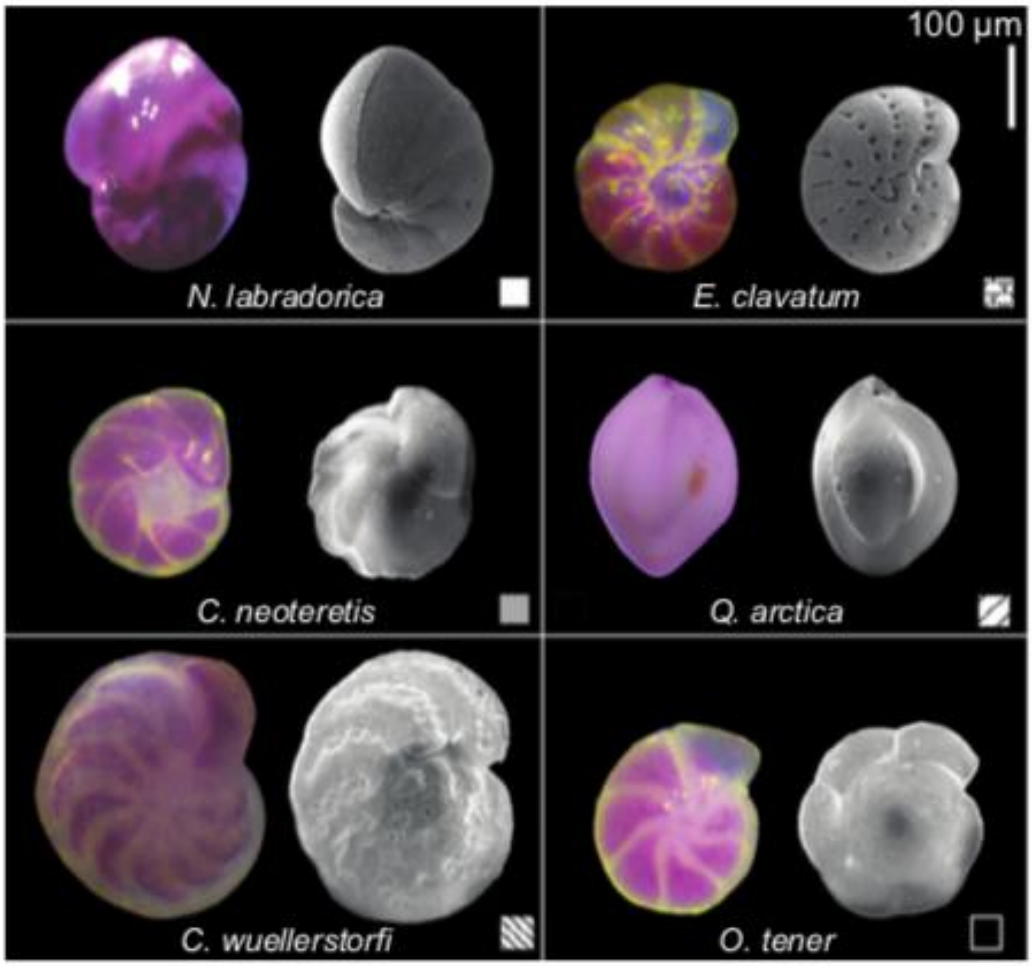


*Figure 2. Image of the most common benthic foraminiferal species in the Arctic: Nonionella labradorica, Elphidium clavatum, Cassidulina neoteretis, Quinqueloculina arctica, Cibicidoides wuellerstorfi and Oridorsalis tener. The pink images are foraminifera with added Rose Bengal. The grey-scaled images are SEM images. The picture is taken from Barrientos et al. (2018).*

## 1.2 Ice-rafted debris (IRD)

Dowdeswell (2009) defines ice-rafted debris (IRD) as “sediment of any grain size that has been transported by floating ice and released subsequently into an aqueous environment”. The sediment can be transported by icebergs or sea ice, or derived from glaciers or ice sheets to marine environments (Dowdeswell, 2009). IRD can also be found in lakes (Dowdeswell, 2009). The grain size of IRD can span from fine silt to large boulders (Dowdeswell, 2009).

IRD are used as palaoceanographic proxies, as they give information about the ice sheet history and evolution in a specific area (Dowdeswell, 2009). In the Northern Hemisphere IRD have been used to reconstruct and explain climatic variations as a response to Earth´s orbitals variations, the ocean-atmosphere interaction, continental movement, and decreasing heat transport to the north (Liu et al., 2018).

The quantity of IRD in marine sediments is equivalent to changes in iceberg distribution (Bond and Lotti 1995; Voelker et al., 2002). During interstadials the value of IRD is lower compared to the values during stadials (Bond and Lotti, 1995; Voelker et al., 2002). This is because the production of icebergs is higher during interstadials then during stadials (Bond and Lotti, 1995; Voelker et al., 2002).

# 2 Regional settings

## 2.1 Svalbard

Svalbard is an Arctic archipelago located between 74° and 81° N, surrounded by the Barents Sea, the North Atlantic and the Arctic Ocean (Figure 3; Dallmann, 2015). The archipelago consists of six large and several small islands (Dallmann, 2015). The total land area is 60 667 km$^2$ (Dallmann, 2015). Glaciers, fjords and mountains dominate the landscape of Svalbard (Dallmann, 2015).

The largest island of Svalbard is Spitsbergen (37 503 km$^2$), followed by Nordaustlandet (14 320 km$^2$), Edgeøya (5009 km$^2$) and Barentsøya (1279 km$^2$) (Dallmann, 2015).


*Figure 3. Map of the Svalbard archipelago (Dallmann, 2015).*

## 2.2 Oceanography

Svalbard is located in the Arctic Mediterranean Sea (Figure 4; Rudels et al., 2014), which consists of the Arctic Ocean and the Nordic Seas (Aagaard et al., 1985). The Nordic Seas are the Greenland, Iceland and Norwegian Sea, also commonly abbreviated to the GIN Sea (Hopkins, 1991). The GIN Sea contains two main water masses: the Polar Water and the North Atlantic Water. The Polar Water derives from the Polar Sea, and the North Atlantic Water derives from the North Atlantic (Hopkins, 1991). The Polar Water is cold and has a low salinity, while the North Atlantic Water is warm and saline (Hopkins, 1991). Sea ice is common on the north, east and south side of Svalbard, where the Polar Water prevails (Dallmann, 2015).

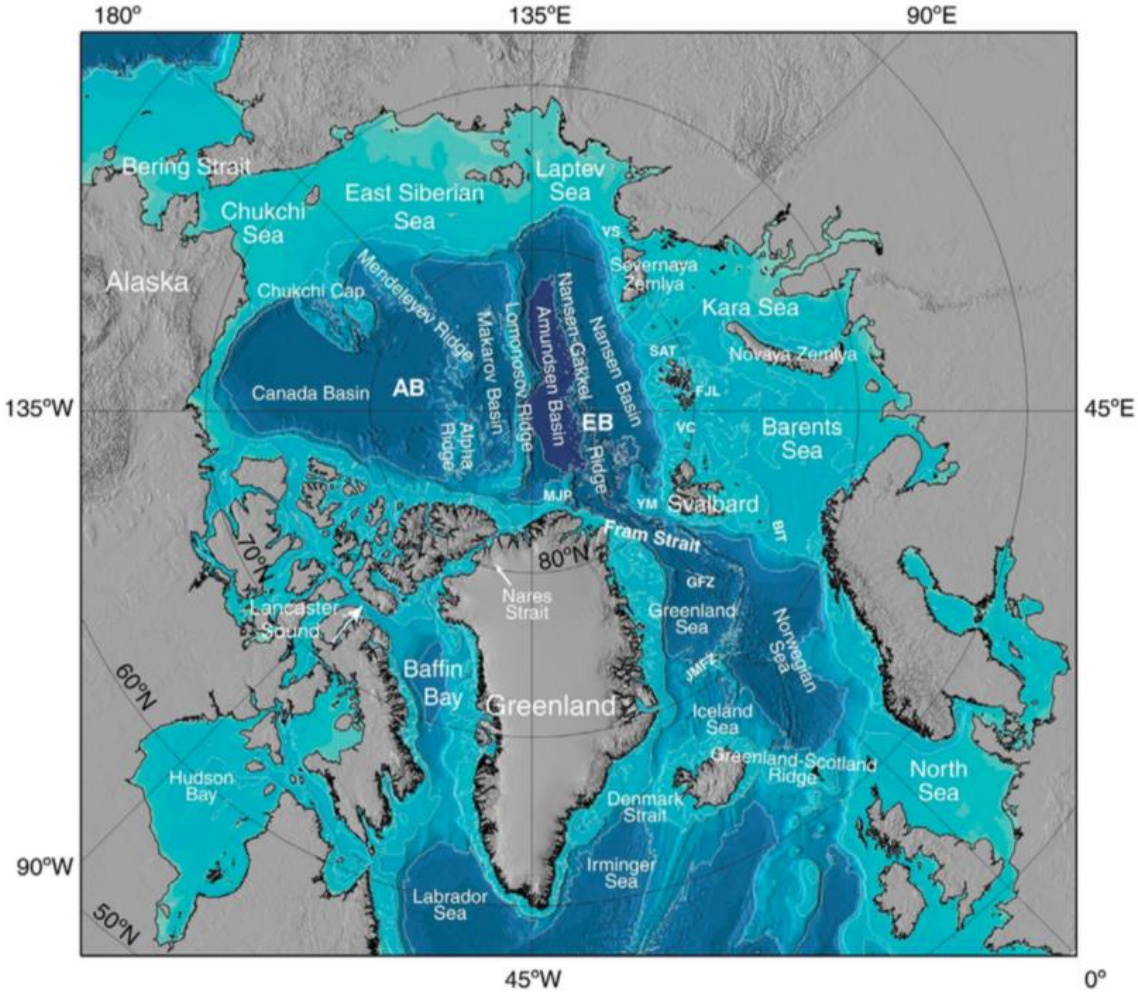


*Figure 4. Bathymetric map of the Arctic Mediterranean Sea (Rudels et al., 2014).*

The Fram Strait is located between northeastern Greenland and Svalbard, (Rudels et al., 2014), which has a maximum water depth of 2600 m (Aagaard et al., 1985). The main heat and water exchange to the Arctic Ocean is through this strait (Saloranta and Haugan, 2001). West Spitsbergen Current (WSC) and the East Greenland Current (EGC) (Figure 5) are the two main currents flowing through the Fram Strait (Saloranta and Haugan, 2001). The EGC is the main outflow source, travelling from north to south on the western part of the Fram Strait (Saloranta and Haugan, 2001). The EGC export the largest amount of sea ice from the Arctic Ocean (Saloranta and Haugan, 2001). The WSC is the main inflow source, travelling from south to north, carrying warm water from the Atlantic into the Arctic on the eastern part of the Fram Strait (Aagaard and Greisman, 1975). The WSC keeps the west coast of Svalbard free of sea ice (Dallmann, 2015).

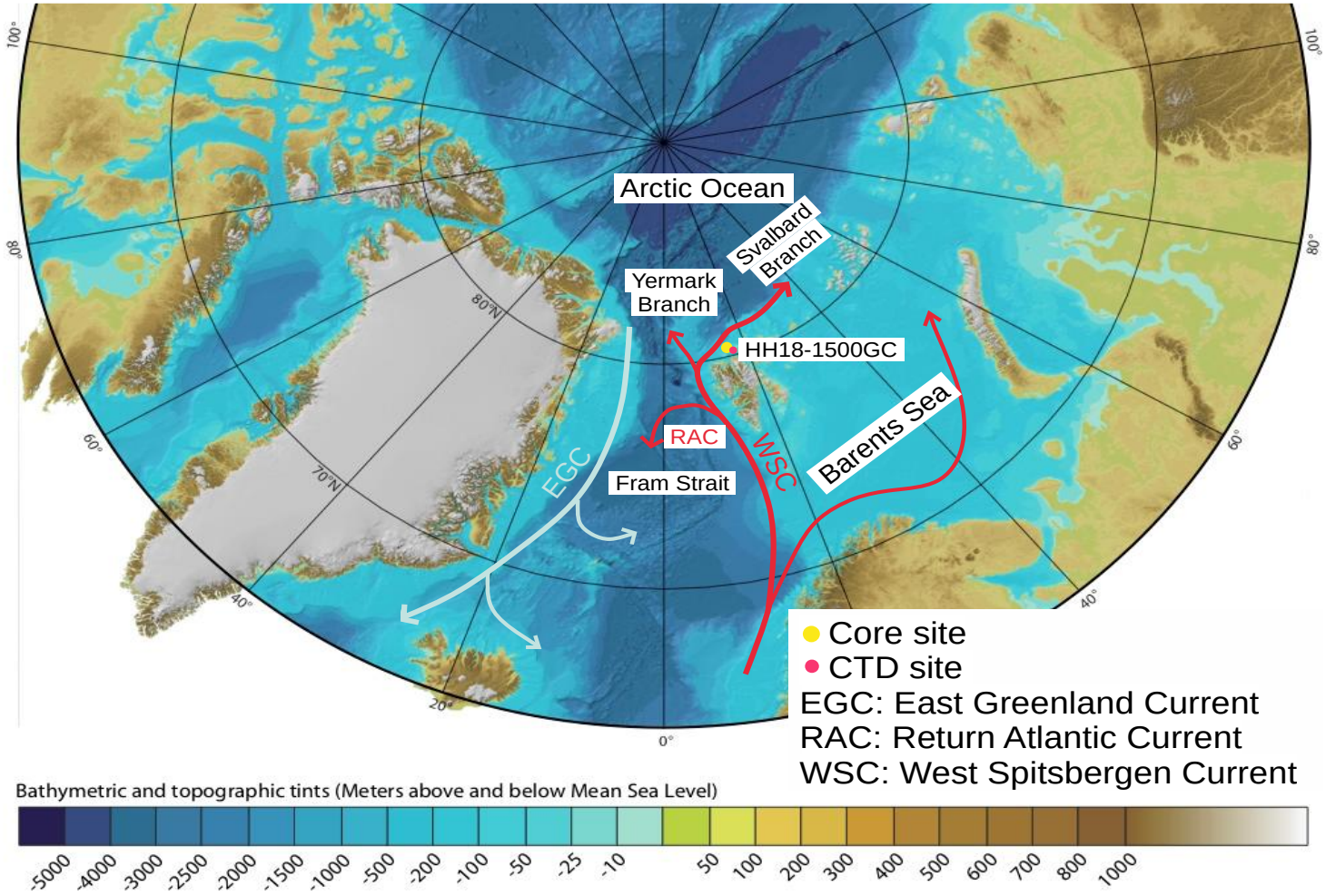


*Figure 5. Map showing the main currents around Svalbard. The core site HH18-1500GC and the CTD site are also marked. Modified from Slubowska et al. (2005).*

When the WSC travels from south to north, some of it stays in the Fram Strait before it is transported southwards by the EGC together with Polar surface water and Arctic Atlantic Water from the Arctic Ocean, as the Return Atlantic Current (RAC) (Figure 5). The rest of the WSC continues to the Yermak Branch, north past the Yermak Plateau, or along the northern Svalbard to the Svalbard Branch (Figure 5). The northward flow in the WSC is estimated to be 6,6 Sv ($1\ Sv = 1 \cdot 10^6\ m^3 s^{-1}$) (Beszycynska-Möller et al., 2012). 3,0 Sv of this flow has a temperature above 2 °C (Beszycynska-Möller et al., 2012). The southward flow in the EGC is larger than the northward flow in the WSC. The EGC transports water of 8,6 Sv (Beszycynska-Möller et al., 2011). This gives a net outflow through the Fram Strait of 2,0±2,7 Sv (Beszycynska-Möller et al., 2011).

The flow through the Barents Sea, which is situated between Svalbard, Russia and the Norwegian main land, also contributes with heat and water in and out of the Arctic Ocean (Figure 5) (Rudels et al, 1999). The heat exchange is of less importance compared to the Fram Strait, but the volume supply from the Barents Sea to the Arctic Ocean is important (Rudels et al, 1999). The inflow though the Barents Sea almost compensates for the net outflow though the Fram Strait (Rudels et al., 2014).

A CTD (conductivity, temperature, depth) profile (Figure 6) was taken at 80.23.836 °N and 16.11.919 °E (Figure 5) during the AMGG cruise 31$^{st}$ of August 2018 to the 12$^{th}$ of September 2018. The CTD correlates with water masses, where the water masses are divided by certain temperature and salinity. On the surface there is a mixed layer of generally cold and fresh water (Hopkins, 1991). Underneath the mixed layer, Polar Water is usually discovered (Slubowska et al., 2005). Subsurface Atlantic water of higher salinity flows below the Polar Water (Slubowska et al., 2005). The mixed layer is within the upper few meters of the water column.The Polar water is believed to be found at < 75 m depth, and the Atlantic water > 75 m depth (Figure 6).

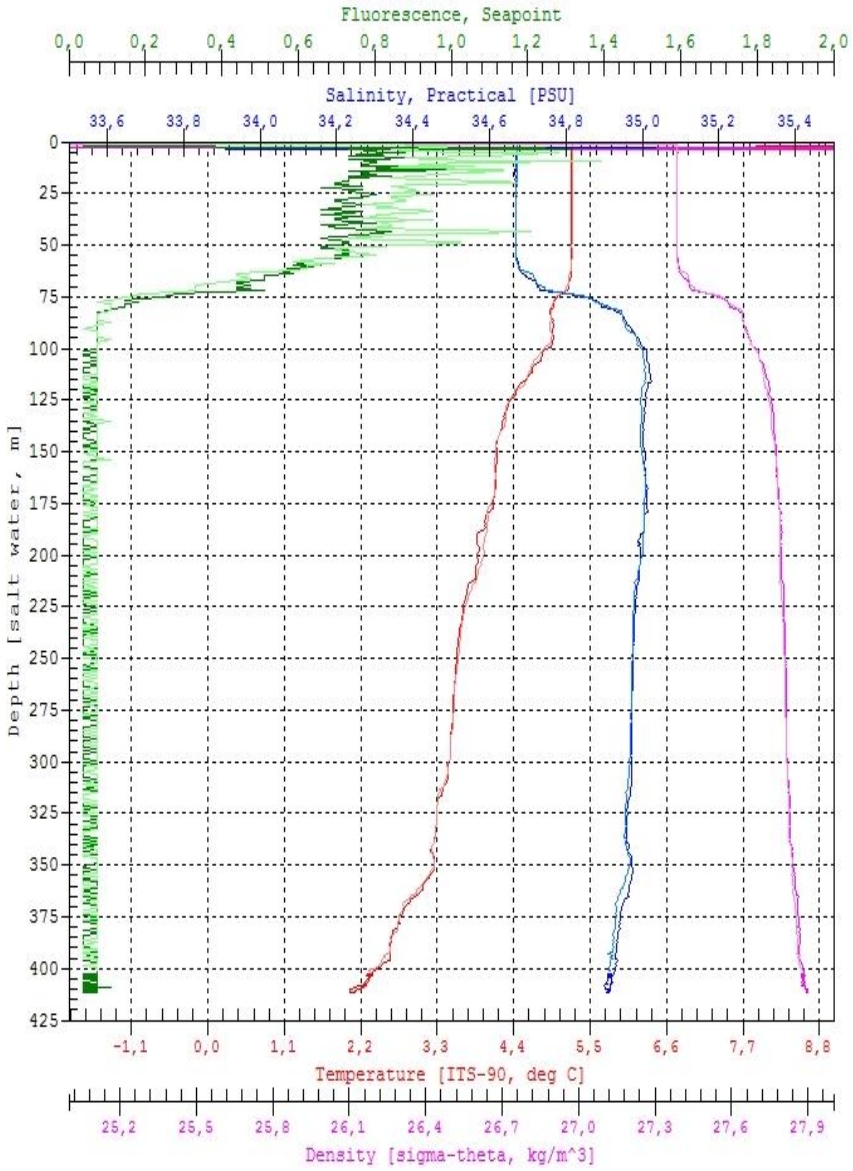


*Figure 6. CTD profile taken on the AMGG cruise. The profile shows the measured fluorescence, salinity, temperature and density by depth at the site.*

## *2.3* Overall geology

The geology of Svalbard contains rocks from all the main geological periods of the Earth (Figure 7; Dallmann, 2015). The bedrock geology of northern Spitsbergen consists of Mesoproterozoic, Neoproterozoic, Devonian, Carboniferous and Permian, and Triassic/middle Jurassic rocks. Some Paleoproterozoic granitic and dolerite rocks are also found. Southern Spitsbergen is mainly Paleogene and Neogene, middle Jurassic/early Cretaceous, and Neoproterozoic rocks. Carboniferous and Permian, Neoptroterozoic, Mesoproterozoic, and granitic rocks are the most common rocks on Nordaustlandet. Triassic/middle Jurassics rocks and dolerite prevail on Edgeøya. On Kvitøya, Mesoproterozoic rocks are the most common (Dallmann, 2015). The Neoproterozoic, Mesoproterozoic and Paleoproterozoic rocks are pink, which is quite common for the sediments around Svalbard (Rasmussen and Thomsen, 2013).

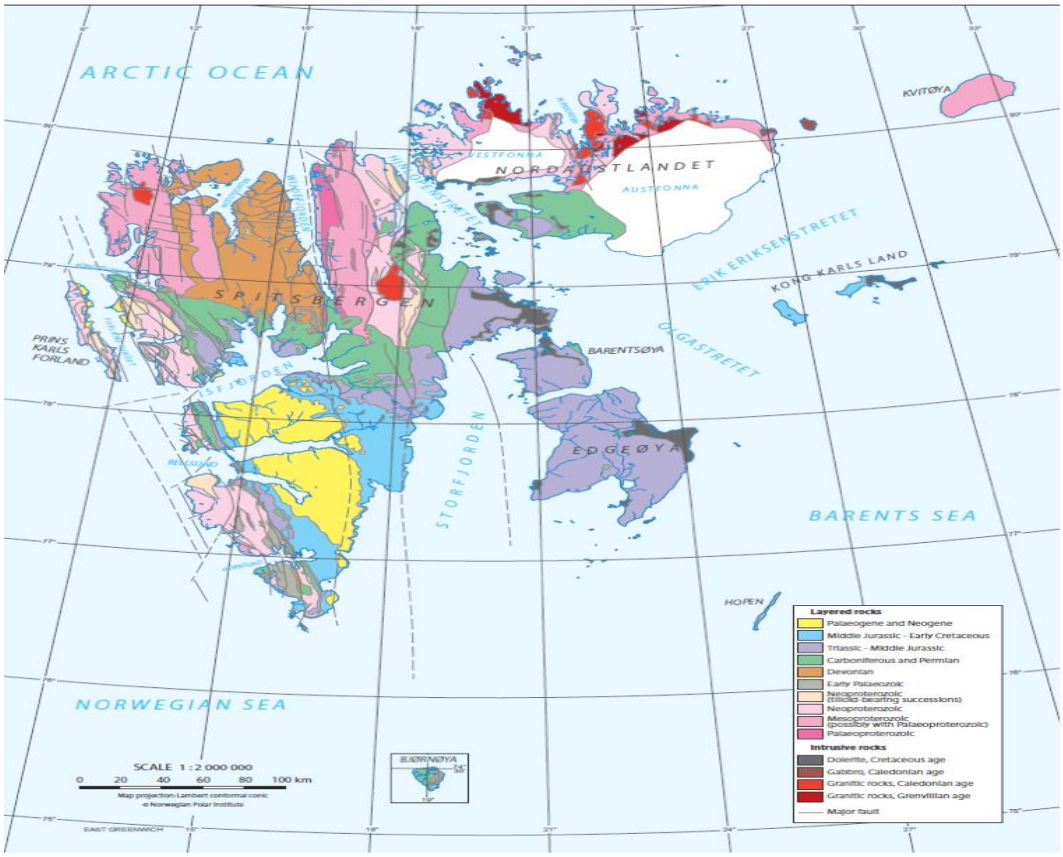


*Figure 7. Bedrock geology of Svalbard (Dallmann, 2015).*

## 2.4 Past climate and paleoceanography of Svalbard

The marine isotope stage 3 (MIS 3) was dated 60 000-25 000 years BP, and consisted of approximately 15 sudden temperature oscillations (Rasmussen and Thomsen, 2013). These temperature oscillations are the Greenland interstadials and stadials (Rasmussen and Thomsen, 2013). An interstadial-stadial event is commonly known as a Dansgaard-Oeschger (DO) event (Dansgaard, 1985). During these DO events, the temperature over Greenland could increase with over 10 °C just within a few years (Dansgaard et al., 1993).

A study from Rasmussen et al. (2006) indicated that the Atlantic water has been present on the southwestern Svalbard shelf over the last 20 000 years. From 15 000 to 10 000 $^{14}$C years BP, the Atlantic water flowed below polar surface water, as a subsurface water (Rasmussen et al., 2006). This period includes the Heinrich event H1, the Bølling-Allerød interstadials and the Younger Dryas stadial (Rasmussen et al., 2006). Studies have shown that during the Bølling-Allerød interstadial, the first flow of warm subsurface Atlantic water after the Last Glacial Maximum took place (Slubowska et al., 2005). Cold and polar conditions were dominating during the Younger Dryas, which is dated c. 11 000-10 000 years $^{14}$C BP (Rasmussen et al, 2006). Svalbard has been highly glaciated since the Pleistoscene (Dallmann, 2015). During the early Holocene, there was an inflow of more saline and cold Atlantic water, which made the biological productivity stronger seasonally (Slubowska et al., 2005). After that, during the mid-Holocene, the inflow of the Atlantic water declined (Slubowska et al., 2005). 7000-8000 years ago the glaciation was at a minimum, while the glaciation was at a maximum c. 2500 years ago, and during the end of the Little Ice Age ($\sim 1870 - 1920$) (Dallmann, 2015). The inflow of Atlantic water have increased the last $\sim$ 1000 years (Slubowska et al., 2005).

In many marine sediments in the Arctic, pink clay has been discovered (Rasmussen and Thomsen, 2013). The pink clay is from sediments from the Devonian Red Beds (Figure 8; Rasmussen and Thomsen, 2013) that were transported in suspension by melt water during warm periods (Rasmussen and Thomsen, 2013) Normally, greenish silt was deposited during interstadials (Rasmussen and Thomsen, 2013).

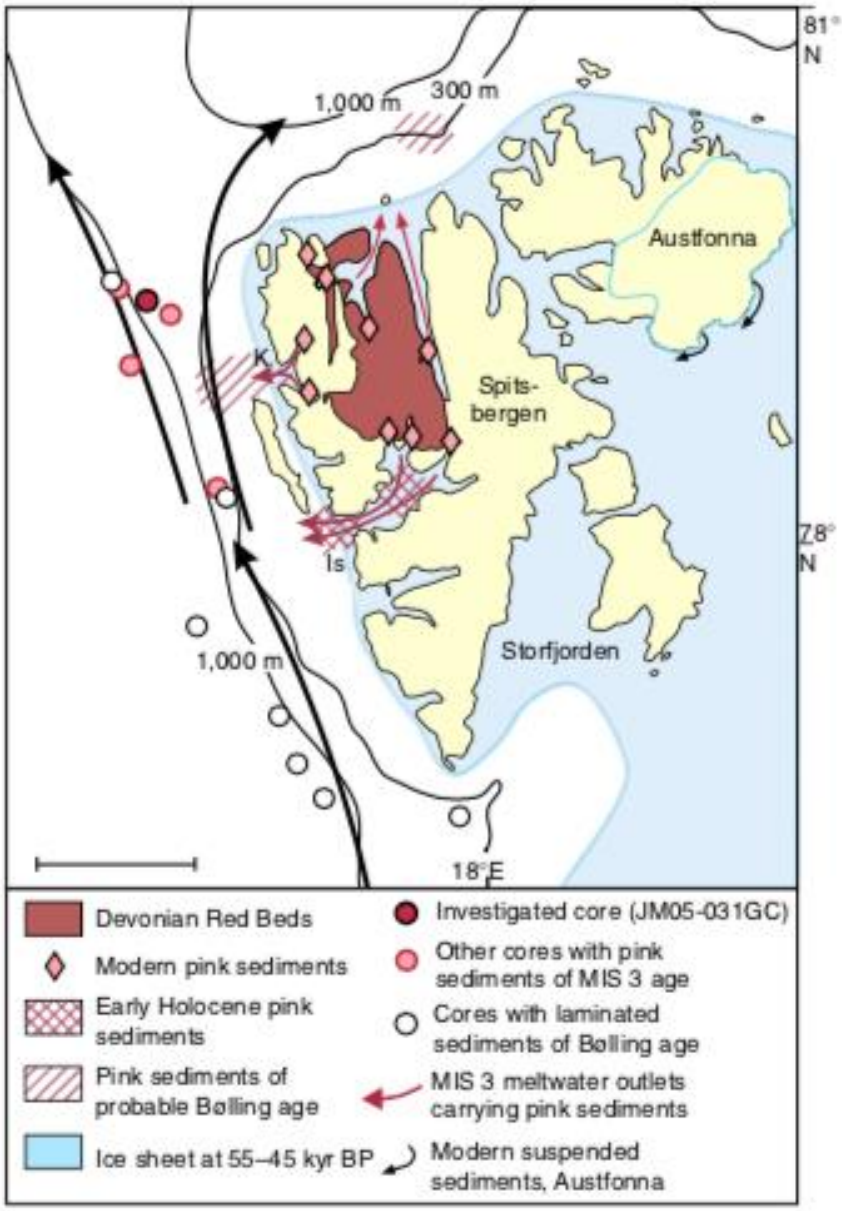


*Figure 8. Location map showing the Devonian Red Beds on Svalbard. The pink arrows illustrates where the MIS 3 melt water are carrying the pink sediments. The pink striped areas are showing sediments of probable Bølling age, while the pink crossed areas are showing sediments of early Holocene. The Hinlopen Trough is located where there are found pink sediments of Bølling age (Rasmussen and Thomsen, 2013).*

# 3 Study area

The Hinlopen Strait is located between the two largest islands of Svalbard: Spitsbergen and Nordaustlandet (Dallmann, 2015). The strait is 110 km long (Ottesen et al., 2007), and was formed by large ice streams (Dallmann, 2015). The Hinlopen Trough is north of the Hinlopen Strait, extending towards the shelf edge (Figure 9; Batchelor et al., 2011). The trough is 5-10 km wide (Ottesen et al., 2007). The maximum water depth of the Hinlopen Strait and Trough is 400 m (Pfirman and Milliman, 1987). Several shelves are dividing the Hinlopen Strait into a number of separated basins (Pfirman and Milliman, 1987). The basins can consist of sediments that are more than 60 m thick. The first 1-5 m of these sediments are of Holocene age, while the sediments below are usually of late Quaternary age (Pfirman and Milliman, 1987).

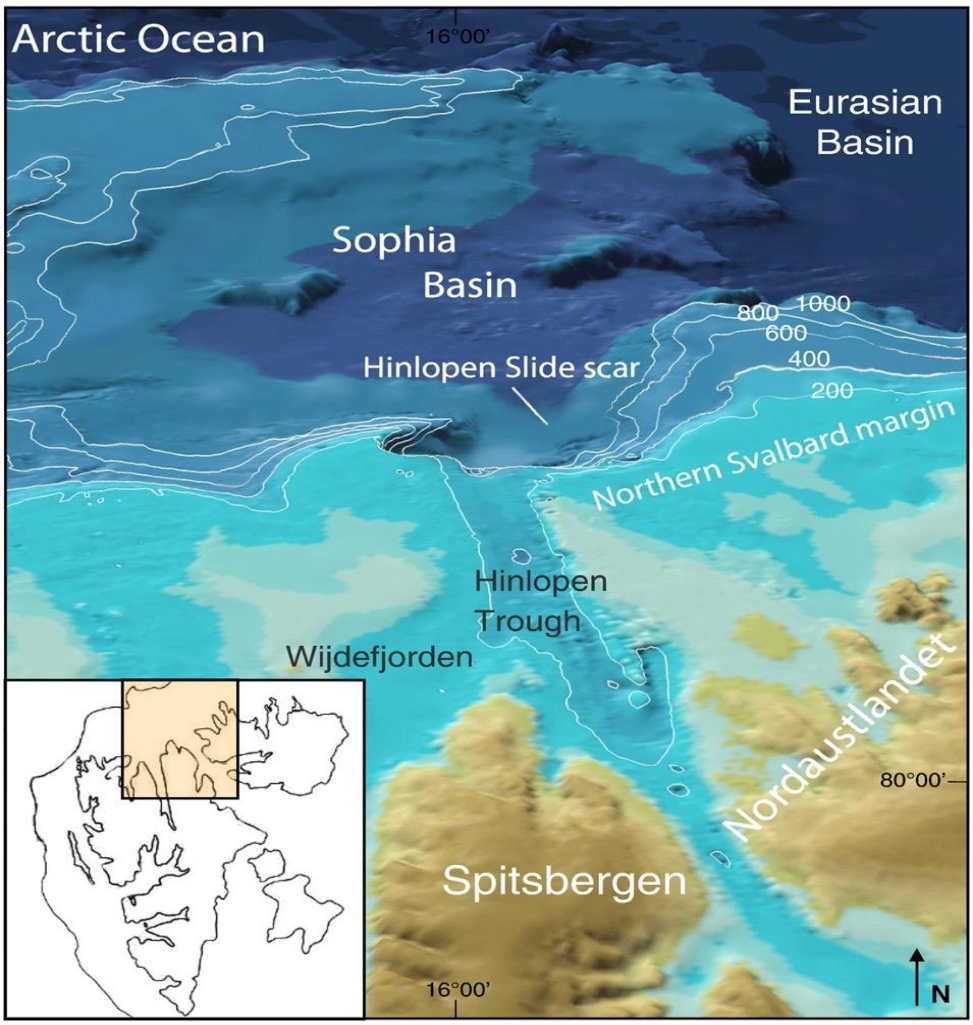


*Figure 9. Bathymetric map of Hinlopen Trough found in Batchelor et al, 2011. The inset is marking the area of study within Svalbard.*

On the continental slope, there has been identified a giant, submarine landslide (Vanneste et al., 2006; Winkelmann et al., 2008). The Hinlopen Slide is one of the largest landslides in the world, with a sediment volume of 1350 $km^3$ (Vanneste et al., 2006). The age of the slide is c. 30 000 years BP (Winkelmann et al., 2008).

Studies have indicated that an ice stream covered the Hinlopen Trough during the Last Glaxial Maximun and the deglaciation (Ottesen et al., 2007; Winkelmann et al., 2008). Drumlins and ice-sculpted bedrock on the sea floor indicate previous presence of ice cover. Dark grey diamict is discovered in megaflues, which is believed to be subglacial till. The deglaciation in the Hinlopen Trough is assumed to be rapid due to lack of grounding-zone features (Batchelor et al., 2011). Since the subglacial bedforms are following the same direction as the known flow direction of the ice stream, the ice-stream flow is considered fast (Clark, 1993; Stokes and Clark, 1999). The rates of debris delivery are calculated to be of 5-7.5 m per thousand years, indicating that the Hinlopen Trough was a major route of transfer of ice and debris during the Last Glacial Maximun and the delgaciation (Batchelor et al., 2011).

Koc et al. (2002) indicate that the ice in the Hinlopen Strait disintegrated between 13 700 and 13 900 $^{14}C$ years BP. 12 600 $^{14}C$ years BP the subsurface Atlantic waters entered the area, and 10 800 $^{14}C$ years BP the sea ice cover retreated together with the opening of the surface waters.

# 4 Material and methods

## 4.1 Fieldwork

Core HH18-1500GC was investigated for this study. It was retrieved from the Northern Hinlopen Trough, northern Svalbard, at 80.27.603 °N and 15.52.759 °E (Figure 10). The core was collected during the AMGG cruise from 31st of August 2018 to the 12th of September 2018. The water depth at the core site was 378 m. The length of the core is measured to be 476 cm.

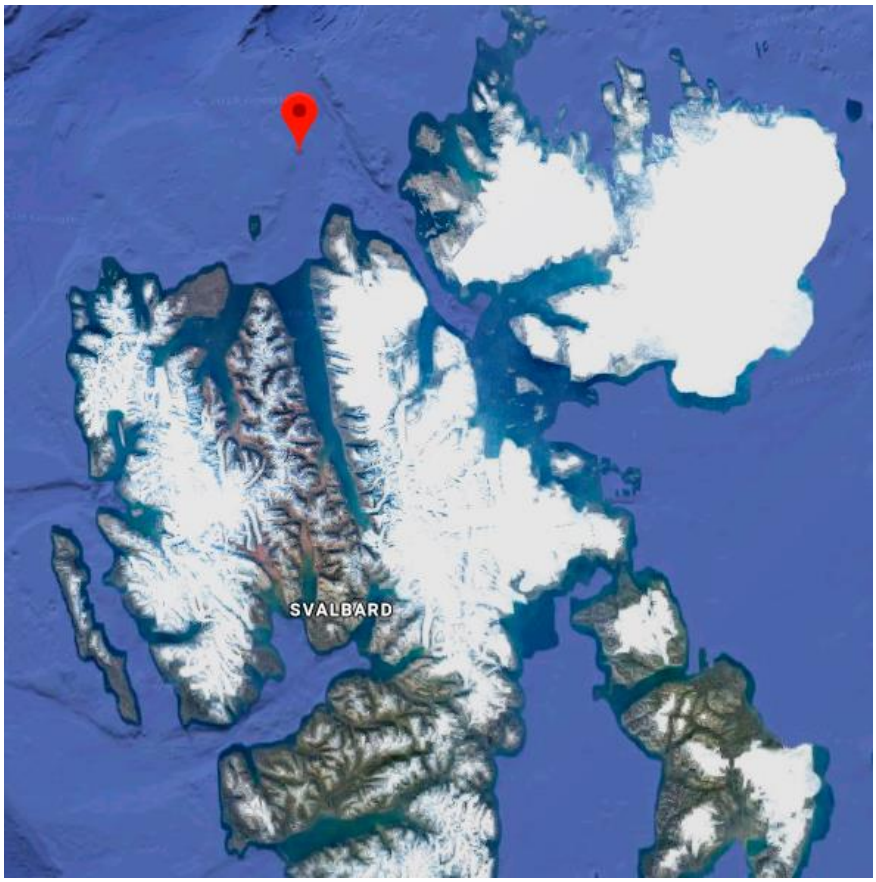


*Figure 10. Location map of the core site HH18-1500GC. The photo was taken from Google Maps with the satellite function, on the 29th of May 2019.*

### 4.1.1 Gravity coring

The core was retrieved using a gravity corer. A gravity corer can be used in water depths up to 3 km, and can collect sediments up to 6 m in thickness. When the gravity corer reaches the ocean floor, it penetrates through the seabed and captures the sediments inside. The force of gravity pulls down the gravity corer. The gravity corer consists of a steel barrier with a plastic tube inside, which is called the core liner. The core cutter, at the end of the gravity corer, is what cuts through the sediments. The core catcher makes sure that the sediments are trapped within the core liner, and the core cutter, at the end of the gravity corer, is what cuts through the sediments. When the gravity corer had collected the sediments, it was lifted up to the vessel again. The core liner was cleaned, measured and labelled before cut into sections of one meter each. The sediments inside the core catcher and the core cutter were stored and labelled.

### 4.1.2 Magnetic susceptibility

Before the core was split in two, the magnetic susceptibility was measured using a GEOTEK loop sensor (Figure 14). The magnetic susceptibility was measured every third centimetre. These measurements allow establishing a preliminary chronological framework of the core since the signal often is correlated with glacial-deglacial events.

### 4.1.3 Splitting the core

The core was split into two halves using a saw and an osmotic knife. The halves were cleaned so that the surfaces were smooth and even. The half that was most perfect was labelled as the archive part, and the other as the work part.

## 4.2 Laboratory work on land

The laboratory work took place in the Department of Geoscience at the University of Tromsø. The core was stored in a cooling room with a temperature around 4 °C when not worked on.

### 4.2.1 GEOTEK Multisensor Core Logger

The GEOTEK Multisensor Core Logger in the Geology laboratory at UiT was used to measure the length of the open core while measuring the magnetic susceptibility and the colour scale every centimetre (Figure 11, Figure 14). Since the work haft of the core was sampled on the cruise, the archive half was used. The core was taken out of the cooling room 24 hours before the logging, so that the temperature of the material could be of room temperature. This was done to avoid any reflections from the surface of the core. Before the logging, the surface of each section was cleaned using plastic cards. The magnetic susceptibility was measured using a point sensor. The colours were given in Munsell values, CIE values, and as spectrophotometer reflectance.

### 4.2.2 Avaatech XRF core scanner

Avaatech XRF core scanner was used to get colour images with high resolution of the five sections (Figure 12). The core was taken out of the cooling room 24 hours before the XRF core scanner was used; i.e. the core needed to be of room temperature and the surface of the core was cleaned. The images from the XRF core scanner show the different features and colouring in the core.

### 4.2.3 GEOTEK X-ray Core-imaging system

The GEOTEK X-ray core-imaging system was used to get grey-scaled X-ray images of the five sections in the core (Figure 13). The core was prepared the same way as for the XRF core scanner; i.e. the core needed to be of room temperature and the surface of the core was cleaned. The grey levels of the images are equal to the density of the core, and the images can be used to determine different sedimentary characteristics, lithological facies, and physical and biological structures (Migeon, et al., 1998).

### 4.2.4 Subsampling and sample preparation

45 sediment samples of 1 cm each were collected from the core. The samples were wet weighed, before they were freeze-dried for 24 hours using Alpha 1-4 LSC plus at the Geology laboratory at UiT. Then the samples were dry weighed. 2-3 g dry sediment was taken out of each sample for TC/TOC analysis (further described in section "1.2.7 TC/TOC"). The samples were washed and sieved using three different sieves of 500 μm, 100 μm, and 63 μm, and then dried within filter papers at 40 °C for 24 hours. The sediments in the filter papers were transferred to drams glasses. The drams glasses were weighed before and after the sediments were transferred, so that the weight of each residue size could be calculated. The empty plastic bags were also weighed so that the total weight of the sediments could be calculated.

### 4.2.5 Grain size analysis

Knowing the weight of the total dry sediment and the weight of each residue size (63-100 µm, 100-500 µm, and >500 µm), the percentages of the different residue sizes in each sediment sample (Figure 15) could be calculated using this procedure:

$$\%\ 63-100\ \mu m = \frac{weight\ of\ 63-100\ \mu m\ residue}{total\ dry\ weight\ of\ sediment\ sample} \cdot 100\%$$

$$\%\ 100-500\ \mu m = \frac{weight\ of\ 100-500\ \mu m\ residue}{total\ dry\ weight\ of\ sediment\ sample} \cdot 100\%$$

$$\%>500\ \mu m = \frac{weight\ of>500\ \mu m\ residue}{total\ dry\ weight\ of\ sediment\ sample} \cdot 100\%$$

$$\begin{aligned} Weight\ of<63\ \mu m\ residue \\ &= total\ dry\ weight\ of\ sediment\ sample \\ &- [(weight\ of\ 63-100\ \mu m\ residue) + (weight\ of\ 100 \\ &- 500\ \mu m\ residue) + (weight\ of>500\ \mu m\ residue)] \end{aligned}$$

$$\%<63\ \mu m = \frac{weight\ of<63\ \mu m\ residue}{total\ dry\ weight\ of\ sediment\ sample} \cdot 100\%$$

These calculations are important because the particle size distribution correlates with changes in sedimentary environment. Due to the Udden-Wentworth scale sediments with particle size <63 µm is defined as silt or clay; particle size 63-100 µm is very fine sand; particle size 100-500 µm is fine to medium sand; and >500 µm is coarse sand, gravel or boulder (Wentworth, 1922).

### 4.2.6 Water content

The water content (in %) of each sediment sample (Appendix 3, Figure 15) was calculated using:

$$Water\ content = \frac{wet\ sediment\ weight - dry\ sediment\ weight}{wet\ sediment\ weight} \cdot 100\%$$

$$= \frac{water\ weight}{wet\ sediment\ weight} \cdot 100\ \%$$

### 4.2.7 TC/TOC

The LECO machine at the Geology laboratory at UiT was used to measure the total carbon and total organic carbon (Figure 15). 2-3 g dry sediment from each sample was put into small steel cups. The steel cups were measured and labelled by depth. The sediments were crushed using an electrical mortar. The crushed sediments were put in ceramic crucibles together with an accelerator and then weighed. After weighing, the crucibles were put in the oven so that the sediment could burn. When the sediments burn, carbon releases and reacts with oxygen, and makes CO and $CO_2$. These are transported to the carbon cells for measuring. $CO_2$ absorbs infrared energy of a known wavelength. The cells consist of an infrared source, and a narrow filter that stops all wavelengths except the wavelength of $CO_2$. When the gasses pass through the cells, they absorb infrared energy and prevent it from reaching the detector. The reduction of energy measured by the detector, is a measure of the concentration of $CO_2$ (Hald, 2017).

To measure total carbon, one analyses the dried sediments directly. When measuring the total organic carbon, one must first add hydrochloric acid to the sediments so that all non-organic carbon is dissolved (Hald, 2017).

The percentage of calcium carbonate (CaCO3) was also calculated (Figure 15). This was done using (Espitalié et al., 1977):

$$(\%\mathrm{TC} - \%\mathrm{TOC}) \cdot 8{,}33$$

### 4.2.8 Foraminifera picking and analysis

From each sample 200-250 benthic foraminifera and all planktonic foraminifera were picked. The samples were usually split one or two times to make the counting easier. The counts were used to estimate the total foraminifera in each sample, the percentage and the concentration of benthic and planktonic foraminifera, and the planktonic/benthic foraminiferal ratio (Appendix 1, Figure 16).

The estimation was found using:

$$\frac{\text{number of forams counted} \cdot 45\ (\text{number of squares})}{\text{counted squares} \cdot \left(\frac{1}{2}\right)^{\text{number of splits}}}$$

The concentration of foraminifera (number/g dry weight sediment) was found using:

$$\frac{\text{equation 1}}{\text{total dry weight of sample}}\ [\text{no./g}]$$

The planktonic/benthic foraminiferal ratio was calculated using:

$$\frac{\text{concentration of planktonic foraminifera}}{\text{concentration of benthic foraminifera}}$$

### 4.2.9 IRD count

The number of IRDs in all of the 45 sediment samples (fraction >500 μm) was counted. The number of IRD per gram (Appendix 2, Figure 16) was calculated using:

$$\frac{number\ of\ IRD\ counted}{total\ dry\ weight\ of\ sample}\ [no./g]$$

### 4.2.10 Radiocarbon dating

Three shells were picked from 188 cm depth, 238 cm depth and 414 cm depth. From the sediment sample at 51.5 cm depth, approximately 700 benthic foraminifera were picked. Each sample was first weighed, then wrapped and sent to CHRONO14 laboratory at Queen University in Belfast, United Kingdom for dating. The years given from Belfast were radiocarbon years. Calib 7.2 Radiocarbon Calibration Program, Marine 13 was therefore used to calibrate the ages into calendar years before present (cal BP) (Table 1).

### 4.2.11 Sedimentation rate

Knowing the calibrated radiocarbon dates at a given depth, the sedimentation rate can be calculated. One must assume that the rates are linear. The sedimentation rates are therefore given by:

$$\frac{depth\ of\ second\ calibrated\ radiocarbon\ date - depth\ of\ first\ calibrated\ radiocarbon\ date}{second\ calibrated\ radiocarbon\ date - first\ calibrated\ radiocarbon\ date}\ [cm/y]$$

The age at a desired depth between two of the calibrated dates can be estimated by:

$$\frac{desired\ depth\ for\ age\ estimation - depth\ of\ first\ calibrated\ date}{sedimentation\ rate\ between\ first\ and\ second\ calibrated\ date} + first\ calibrated\ date$$

If the desired depth is before the first calibrated date or after the last, one must assume that the sedimentation rate is the same as the calculated sedimentation rate between the two closest datings.

Using this, the age at a desired depth above the first calibrated radiocarbon date can be estimated by:

$$age\ of\ closest\ date - \frac{depth\ of\ closest\ date - desired\ depth}{sedimentation\ rate\ between\ the\ two\ closest\ dates}$$

The age at a desired depth below the last calibrated radiocarbon date can be estimated following by:

$$\frac{desired\ depth - depth\ of\ closest\ date}{sedimentation\ rate\ between\ the\ two\ closest\ dates} + age\ of\ closest\ date$$

### 4.2.12 Flux calculations

The flux is given by the concentration multiplied with the mass accumulation rate. The calculation of flux of planktonic and benthic foraminifera, and IRD (Appendix 3, Figure 17) was carried out by following procedure:

The sediment samples were approximately 1 cm thick. The sediment samples are half cylinders, and the volume of the sediment samples are therefore given by:

$$volume\ of\ wet\ sediment\ [cm^3] = \frac{volume\ of\ a\ cylinder}{2} = \frac{\pi r^2 h}{2}$$

where r is the radius (in cm) and h is the height/thickness (in cm) of the sediment samples. The diameter of the core is 10 cm, giving a radius of 5 cm. The mean thickness was 1 cm. This gives a mean volume of 39.267 $cm^3$.

The volume of the sediment samples were used to calculate sediment porosity, wet bulk density and furthermore the dry bulk density:

$$sediment\ porosity\ \left[\frac{g}{cm^3}\right] = \frac{wet\ sediment\ weight - dry\ sediment\ weight}{volume\ of\ wet\ sediment} = \frac{water\ weight}{volume\ of\ wet\ sediment}$$

$$wet\ bulk\ density\ [g/cm^3] = \frac{wet\ sediment\ weight}{volume\ of\ wet\ sediment}$$

$$dry\ bulk\ density\ [g/cm^3] = wet\ bulk\ density - sediment\ porosity$$

The dry bulk density is used to calculate the mass accumulation rate, which is given by:

The flux of planktonic and benthic foraminifera, and IRD was calculated. The flux is given by:

$$MAR = linear\ sedimentation\ rate\ (LSR)\ [cm/ky] \cdot dry\ bulk\ density\ [g/cm^3]$$

where linear sedimentation rate is found by:

$$LSR = sedimentation\ rate\ [cm/y]\ \cdot 1000$$

The reason why the sedimentation rate is multiplied by 1000 is because the linear sedimentation rate is the sedimentation rate every thousand year ($cm/ky$).

The final equation for flux is given by:

$$Flux\ [no./cm^2 ky^{-1}] = concentration\ [no./g]\ \cdot mass\ accumulation\ rate\ (MAR)\ [g/cm^2 ky^{-1}]$$

# 5 Results

The lithological log with correlating XRF and X-ray images is presented in Figure 11. The XRF images and the X-ray images are additionally presented in Figure 12 and Figure 13, giving a more detailed observation.

Magnetic susceptibility, lightness and redness are presented together with the XRF images, X-ray images and the lithological log in Figure 14. The magnetic susceptibility was measured by loop sensor on-board of R/V Helmer Hanssen, and by point sensor at the UiT Geology Laboratory (Figure 14). The graphs show the same tendency throughout the core. This demonstrates that the loop sensor give a good indication of the magnetic susceptibility, which may be important when splitting the core. The values of magnetic susceptibility in the result part will be the values given by the point sensor. At the section ends, the sensors measure extremely low or high values of magnetic susceptibility. This is an error, and the values at these depths are therefore not taken into consideration. This also goes for the redness and lightness, as they are measured by the same point sensor as the magnetic susceptibility.

The grain size fraction, the water content, and the percentages of total carbon, total organic carbon and calcium carbonate are combined with the lithological log in Figure 15. Figure 16 presents the benthic and planktonic foraminiferal concentration, the planktonic/benthic foraminiferal ratio, and the number of IRD per gram sediment together with the lithological log. The flux of benthic foraminifera, planktonic foraminifera and IRD are combines with the lithological log in Figure 17. Table 1 presents the three shells and one assemblage of benthic foraminifera that were dated by AMS radiocarbon. The dates were calibrated to calendar years before present.

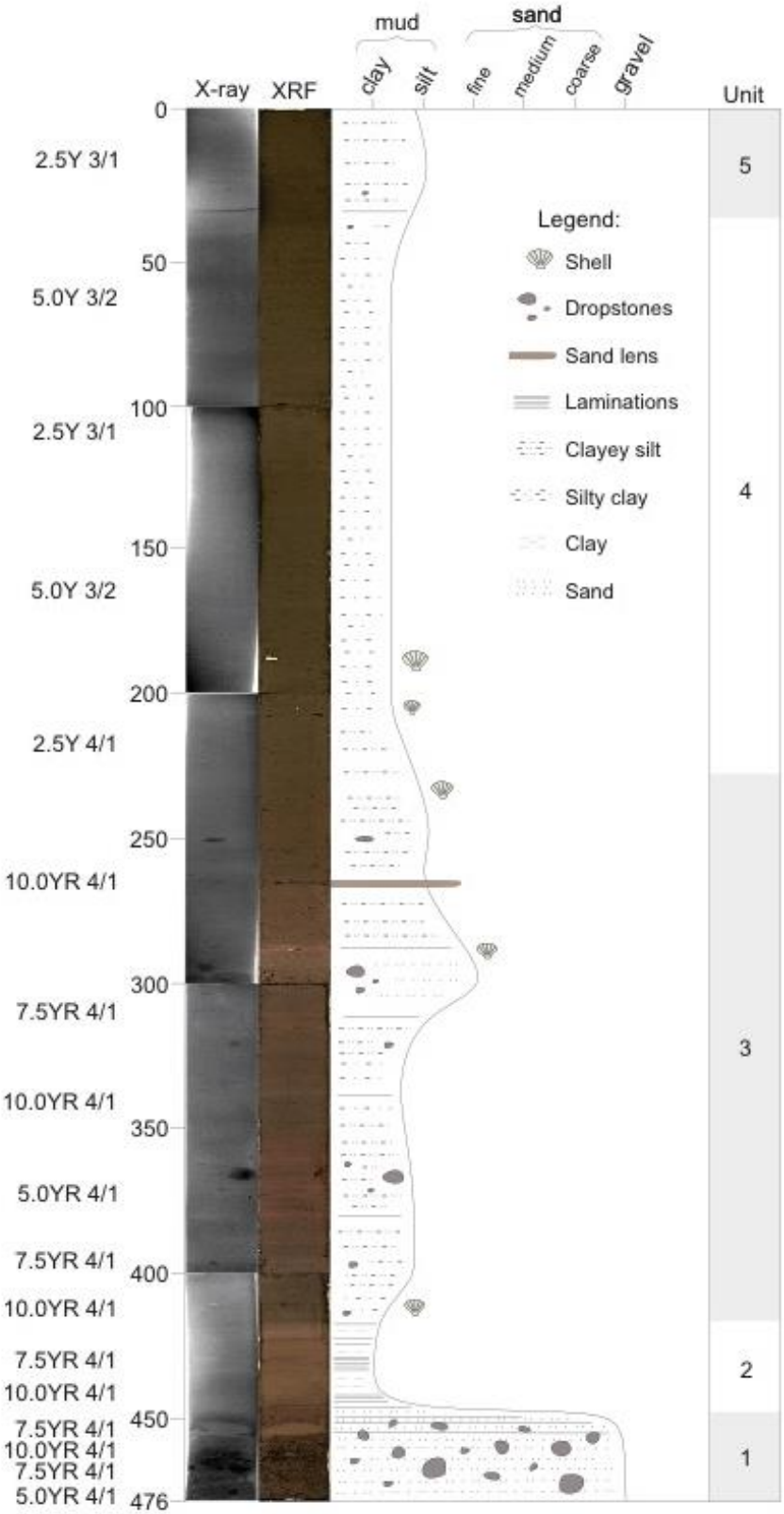


*Figure 11. The lithological log together with corresponding XRF and X-ray images. The core is divided into 5 units. The colour of the core is given in Munsell values.*

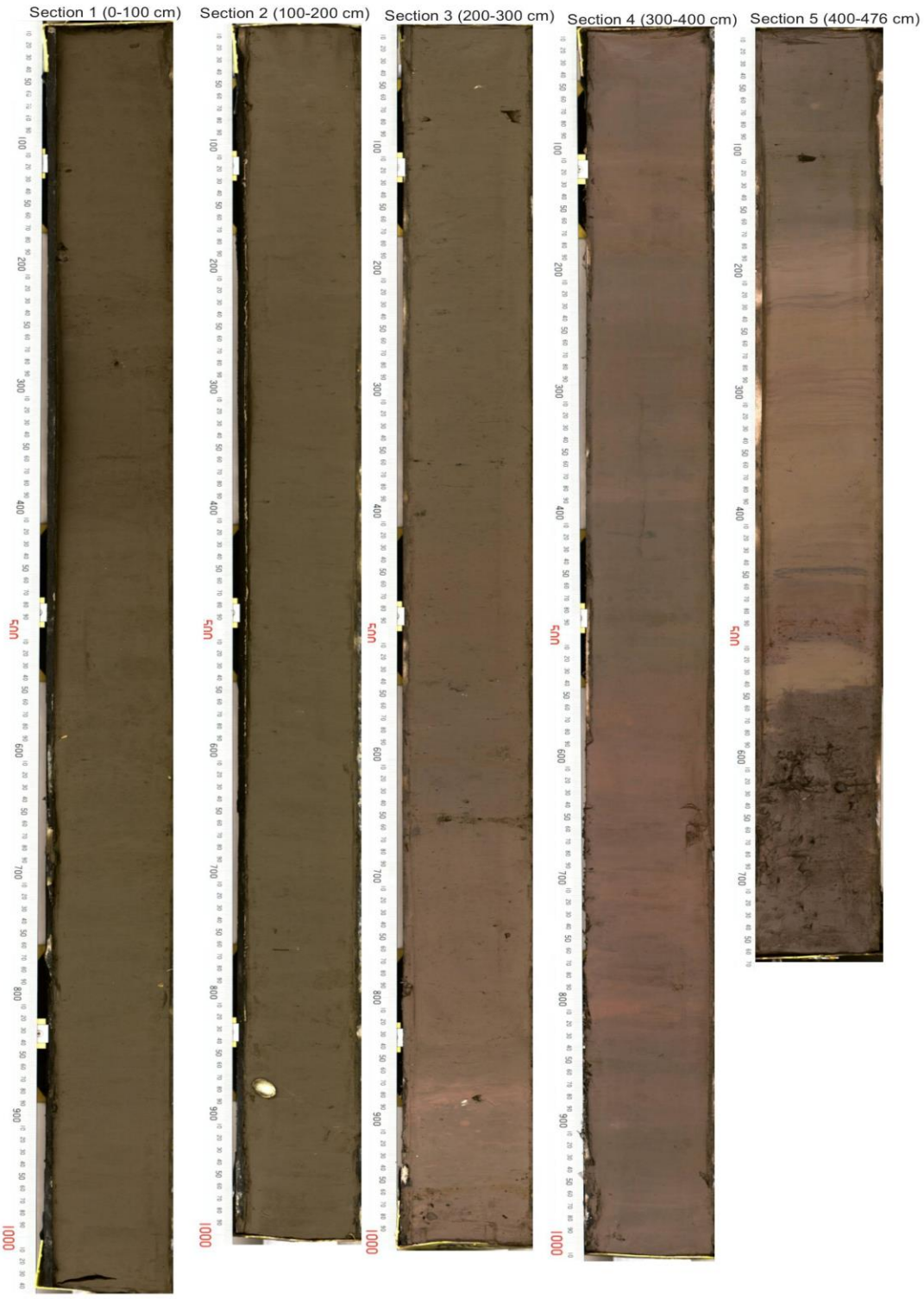


*Figure 12. Images of the five sections of the core taken with Avaatech XRF core scanner. The ruler shows the length (in mm) of the different sections.*

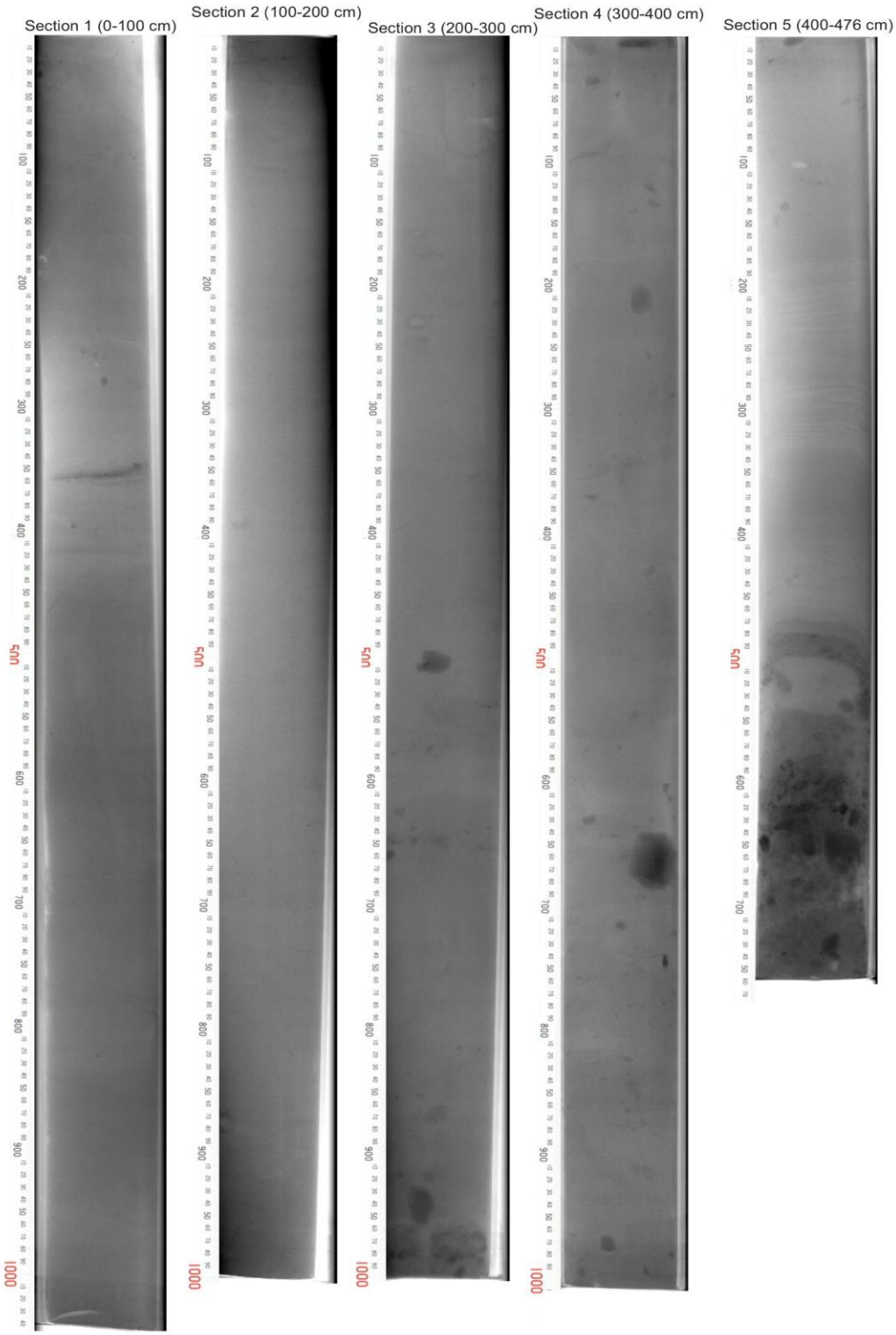


*Figure 13. Images of the five sections in the core taken with the GEOTEK X-ray core imaging system. The ruler shows the length (in mm) of the different sections*

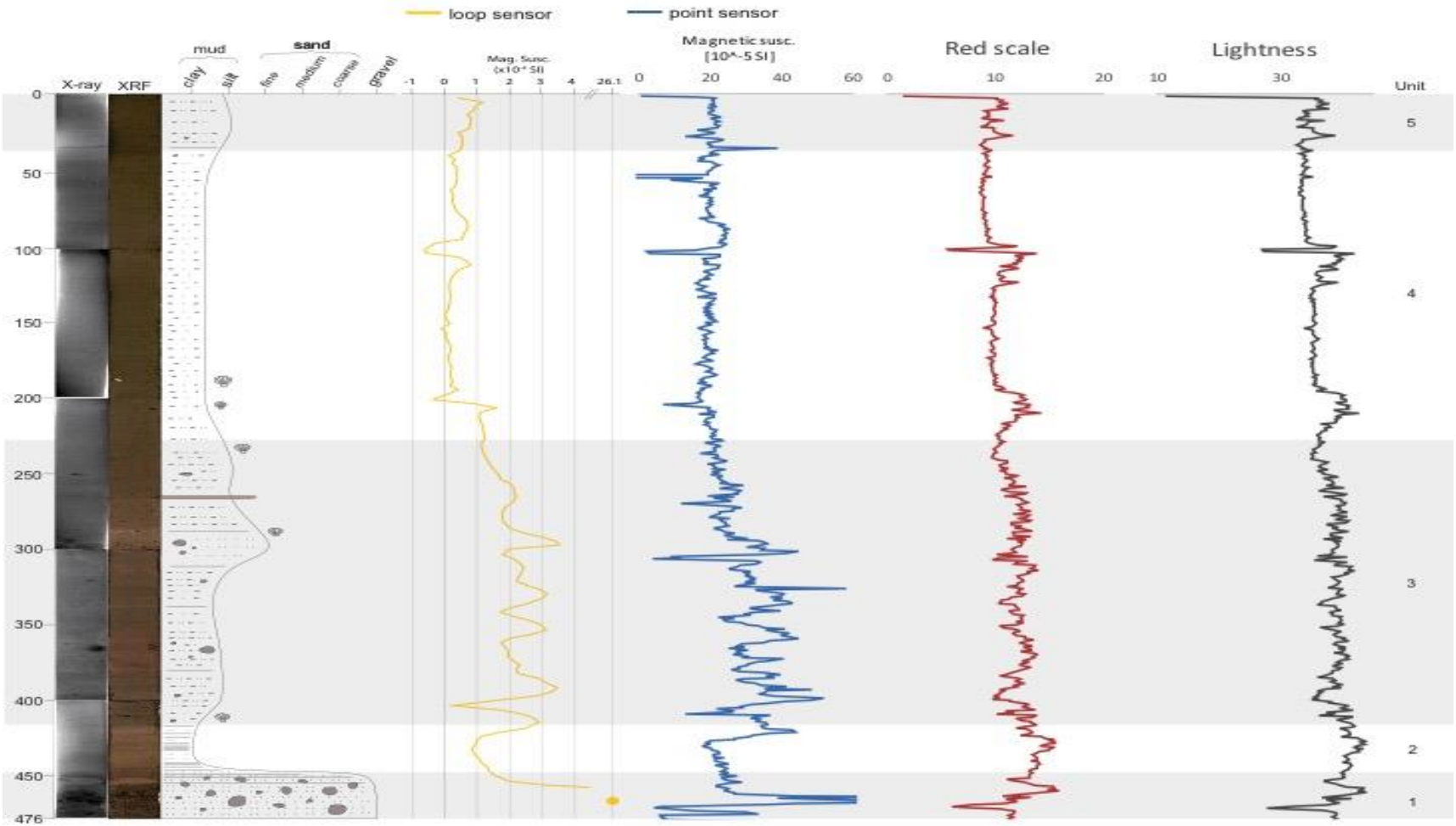


*Figure 14. X-ray and XRF images together with the lithological log, magnetic susceptibility measured by loop sensor (yellow graph) and by point sensor (blue graph), red scale and lightness of the different unit*

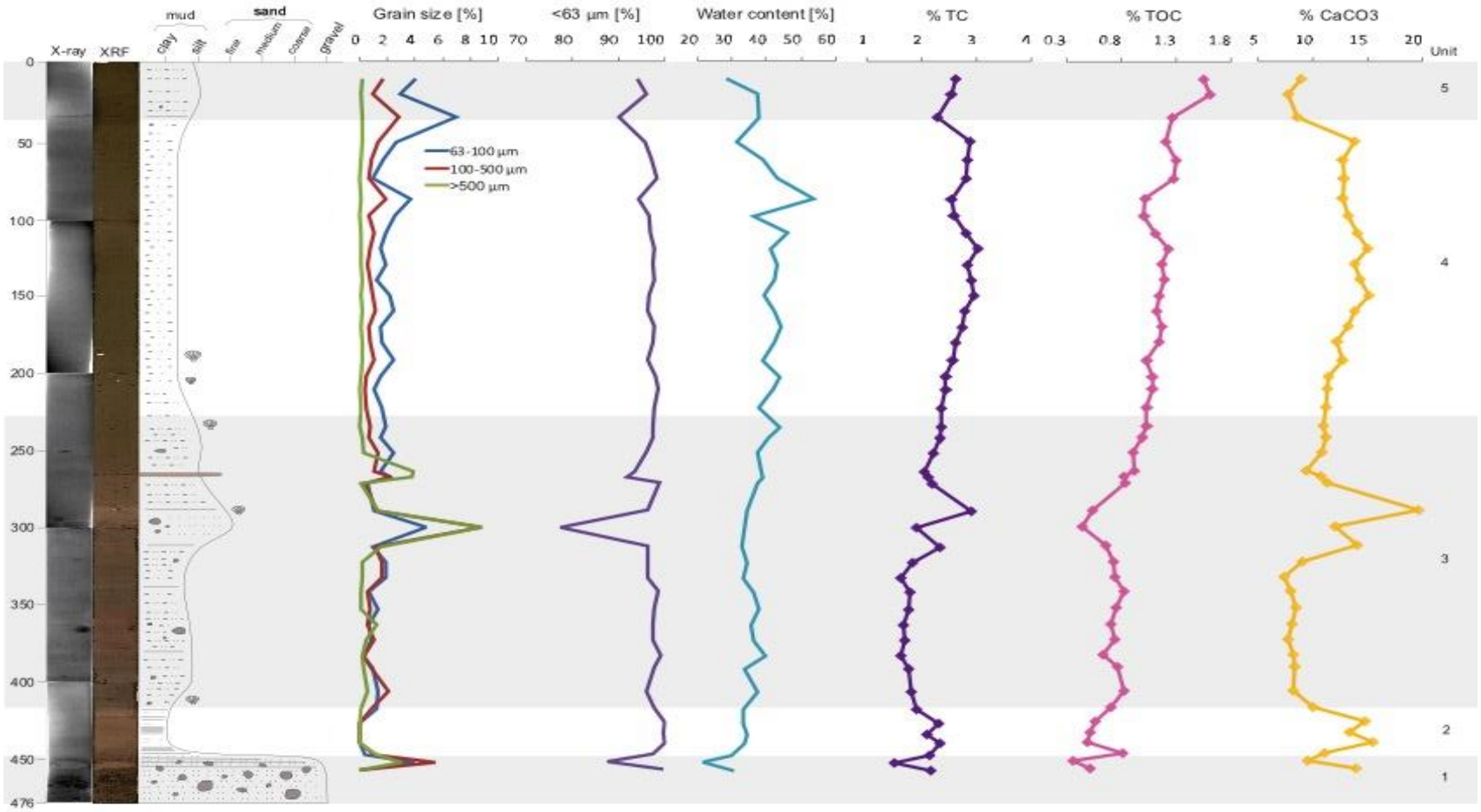


*Figure 15. X-ray and XRF images together with the lithological log, grain size distribution, water content, percentage of total carbon (TC), total organic carbon (TOC) and calcium carbonate ($CaCO_3$) of the different units.*

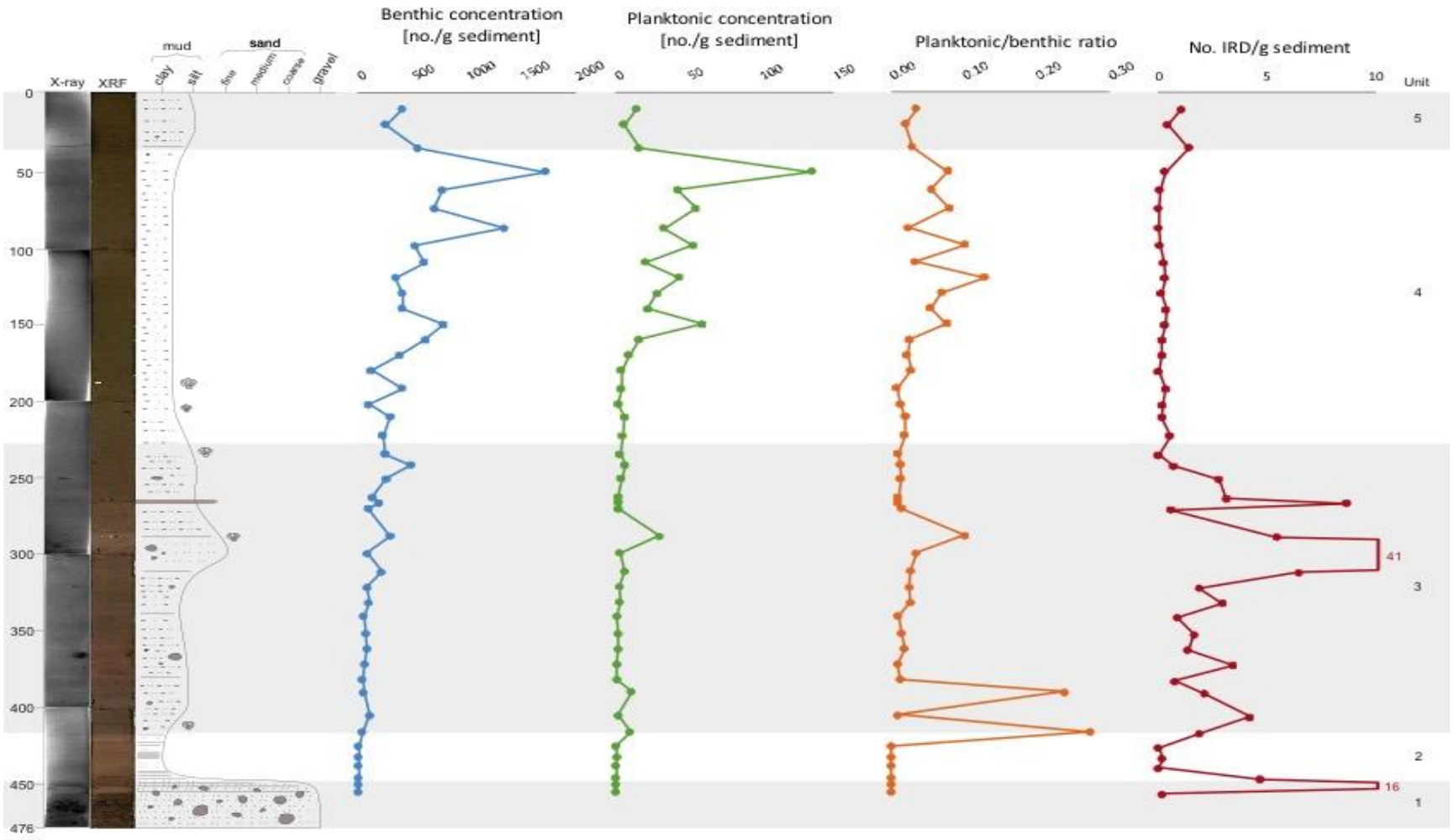


*Figure 16. X-ray and XRF images together with the lithological log, the concentration of benthic and planktonic foraminifera, the planktonic/benthic foraminiferal ratio, and the number of IRD per gram sediment of the different units.*

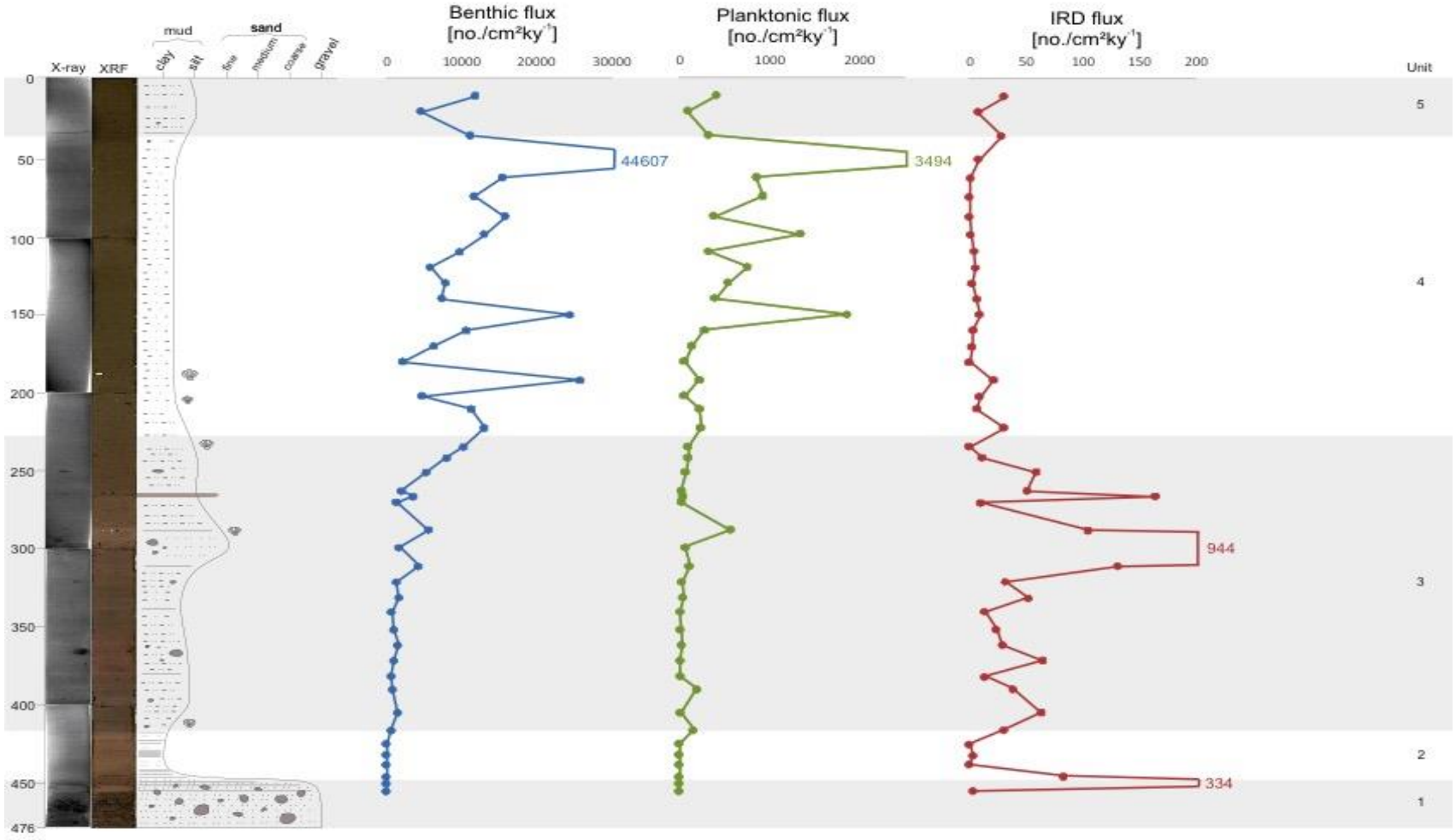


*Figure 17. X-ray and XRF images together with the lithological log, the flux of benthic and planktonic foraminifera, and the flux of IRD of the different units.*

| Depth | Material type | Sample weight | Radiocarbon years | Cal years BP | Cal years BP mean |
|---|---|---|---|---|---|
| 51.5 cm | Benthic foraminifera | 26.40 mg | 7054±46 | 7578-7491 | 7534.5 |
| 188 cm | Bathyarca glacialis (bivalve) | 102.9 mg | 9400±30 | 10 253 - 10 188 | 10 220.5 |
| 238 cm | Bathyarca glacialis (bivalve) | 62.80 mg | 9740±31 | 10 683 - 10 586 | 10 634.5 |
| 414 cm | Unknown (bivalve) | 15.70 mg | 13245±45 | 15 384-15 197 | 15 290.5 |

*Table 1. The four radiocarbon datings of core HH18-1500GC. The ages are calibrated using Calib 7.2 Radiocarbon Calibration Program, Marine 13.*

## 5.1 Unit 1 (476-445 cm depth)

Unit 1 is found from the bottom of the core to a depth of approximately 445 cm (Figure 11). This unit consists of unsorted, matrix supported gravel and sand, typical of 'till' or material deposited in front of an ice-grounding zone (Nielsen and Rasmussen, 2018). The colouring changes from 5.0YR 4/1 at the bottom of the unit, to 7.5YR 4/1 and 10.0YR 4/1. These colour values are all named brownish grey, there 5.0YR is slightly redder than 10.0YR. In the upper part of the unit, thin laminations are discovered (Figure 11). The dark spots in the X-ray images indicate drop stones and coarse material (Figure 13).

The highest values of magnetic susceptibility are measured in unit 1 (Figure 14). At 467 cm depth the value is $97.1*10^{-5}$ SI, and at 464 cm depth the value is $.92.2*10^{-5}$ SI. From this point, the magnetic susceptibility decreases toward the unit above.

Higher values in the redness graph may indicate pink layers (Figure 14). At 470 cm depth, the redness is at its lowest, ignoring the values measured at the section ends, being approximately 6 %. The highest value of redness is measured to be 13.32 %. This value is found at 460 cm depth. The lightness follows the exact same pattern as the redness, varying from approximately 28 % at the lowest, to 41.47 % at the highest (Figure 14).

The only two sediment samples taken out from unit 1 were located in the upper part of the unit. This makes the results regarding water content, total carbon, total organic carbon, calcium carbonate (Figure 15), IRD (Figure 16 and Figure 17) and foraminifera (Figure 16 and Figure 17) sparse. At 453 cm depth, the water content is approximately 30 % (Figure 15). From 453 to 448 cm depth, the water content decreases to 20 %.

The percentage of total carbon at 453 cm depth is approximately 2 (Figure 15). From this depth, the percentage decreases to 1.5 at the top of the unit, which is the lowest percentage of total carbon measured in the core. The percentage of total organic carbon follows the same pattern as the total carbon, decreasing from 0.5 to approximately 0.35 % (Figure 15). The calcium carbonate content decreases from approximately 14 % to 9.5 % (Figure 15).

The number of benthic and planktonic foraminifera per gram dry weight sediment is approximately 0 (Figure 16). The number of IRD per gram sediment increases from 0 to 16,

before it decreases towards unit 2 (Figure 16). The IRD flux follows the same pattern as the IRD/g, increasing from 2 to 334 no./$cm^2k^{-1}$ (Figure 17).

## 5.2 Unit 2 (445-420 cm depth)

Unit 2 consists of clay (Figure 11, Figure 15). Thin laminations are discovered within the whole unit. The colour changes between 10.0YR 4/1 and 7.5YR 4/1 (brownish grey) (Figure 11). The water content increases from approximately 21 % at the bottom of the unit, to 34 % in the upper part (Figure 15).

The magnetic susceptibility in unit 2 is relatively low (approximately $20*10^{-5}$ S) (Figure 14).

The redness of unit 4 is relatively stable, being around 13-14 % (Figure 14). The lightness varies between 40 and 41% (Figure 14). At approximately 430 cm depth, both graphs peak values of 15.47 % redness and 43.3 % lightness. At this depth, the lithological log combined with the X-ray and XRF images, there is discovered a pinkish layer (Figure 11, Figure 14).

The percentages of total carbon and calcium carbonate are relatively high in unit 2, being respectively approximately 2.3 and 13-15 (Figure 15). The percentage of total organic carbon is, on the other hand, relatively low. The total organic carbon decreases to 0.5 % (Figure 15).

The number of benthic and planktonic foraminifera per gram dry weight sediment is approximately 0 (Figure 16). The number of IRD per gram sediment decreases from 5 at the bottom, to more or less zero (Figure 16). The IRD flux decreases from 80 no./$cm^2k^{-1}$ to approximately 0 (Figure 17).

## 5.3 Unit 3 (420-225 cm depth)

Unit 3 consists mainly of clayey silt (Figure 11, Figure 15). From approximately 310 to 290 cm depth, there is a subunit consisting of sand (Figure 11, Figure 15). At approximately 260 cm depth, a sand lens is detected (Figure 11). Drop stones are discovered sporadically within the unit (Figure 11, Figure 13). At 414, 288.5 and 238 cm depth, shells are discovered (Figure 11, Figure 12). The bivalve shells at 414 and 238 cm depth, was sent for dating (Table 1). The colouring at the bottom of the unit is 10.0YR 4/1 (Figure 11). Further up it shifts to 7.5YR 4/1. From approximately 388 to 360 cm depth, there appears to be a layer of predominantly pink sediments (Figure 14). The Munsell value of this layer is 5.0YR 4/1 (Figure 11). After this, the colouring changes between 10.0YR 4/1 and 7.5YR 4/1. In the upper part of the unit, the colour shifts to yellowish grey (2.5Y 4/1). The water content is varying from 33 to 43 % (Figure 15). The water content reaches its highest value just below unit 4.

The magnetic susceptibility varies between lower and higher values (Figure 14). At 326 cm depth, the magnetic susceptibility is $58.1*10^{-5}$ SI, which is the third highest measured value in the core. At 307 cm depth, the magnetic susceptibility is $3.7*10^{-5}$, which is one of the lowest values measured. From approximately 250 cm depth, the magnetic susceptibility is more stable (approximately $20*10^{-5}$ SI).

The redness in unit 3 is varying from 11-14 % (Figure 14). The value of red is relatively higher at 395-385 cm depth, 380-360 cm depth, 350-340 cm depth, 315-310 cm depth and 290-260 cm depth. These higher values of red are corresponding with the pinkish layers shown in the XRF images (Figure 12). The lightness shows the same tendency, varying from 36-41 % (Figure 14).

In unit 3, the percentages of total carbon, total organic carbon and calcium carbonate all increase gradually from the bottom of the unit towards the top, except at approximately 320-270 cm depth (Figure 15). In the 320-270 cm depth interval, the total carbon and the calcium carbonate content increase notably, while the total organic carbon decreases. The total carbon and the calcium carbonate peak to values of 2.9 % and 19.6 %, receptively. The total organic carbon reaches a value of 0.45 % at its lowest.

The concentration of benthic foraminifera increases from 0 at the bottom of the unit to 75 no. per gram sediment at 320 cm depth (Figure 16). The benthic foraminiferal flux increases from

570 no./cm$^2$k$^{-1}$ at bottom to 1300 no./cm$^2$k$^{-1}$ (Figure 17). Toward the top the unit, the benthic foraminiferal concentration varies between 75 no./g to 478 no./g (Figure 16). The benthic foraminiferal flux from 320 to 260 cm depth is varying from 1300 no./cm$^2$k$^{-1}$ to 5600 no./cm$^2$k$^{-1}$ (Figure 17). Toward the top of the unit, the benthic foraminiferal flux increases to a value of approximately 12 000 no./cm$^2$k$^{-1}$. The planktonic foraminiferal concentration is more of less stable, varying from approximately 0 to 11 no./g (Figure 16). At 290 cm depth, the concentration peaks to 30 no./g. The planktonic foraminiferal flux graph does not indicate large variations (Figure 17). The flux is varying from 10 to 100 no./cm$^2$k$^{-1}$, except at 290 cm depth where the flux peaks to 570 no./cm$^2$k$^{-1}$.

The planktonic/benthic foraminiferal ratio is generally varying between 0 and 0.03 (Figure 16). The ratio indicates how many planktonic foraminifera there are per benthic foraminifera. When the ratio is below 1, there are more benthic than planktonic foraminifera. The ratio peaks at the bottom of the unit, at 390 cm depth and 290 cm depth, being respectively 0.27, 0.24 and 0.1.

The number of IRD per gram sediment is mainly varying between 1 and 9 (Figure 16). At 300 cm depth, the number reaches 41, which is the highest value throughout the core. The IRD flux is generally varying from approximately 12 to 64 no./cm$^2$k$^{-1}$ (Figure 17). Exceptions are at 265 and 300 cm depth, where the IRD flux reaches 164 no./cm$^2$k$^{-1}$ and 944 no./cm$^2$k$^{-1}$, respectively.

## 5.4 Unit 4 (225-35 cm depth)

Unit 4 consist of silty clay (Figure 11, Figure 15). Two shells are discovered at 205 and 188 cm depth (Figure 11, Figure 12). The bivalve shell at 188 cm depth was sent for dating, together with a collection of benthic foraminifera (Table 1). The lower part of this unit is yellowish grey (2.5Y 4.1) (Figure 11). Then the colouring shifts to olive black (5.0Y 3/2). Further up it changes to brownish black (2.5Y 3/1), before it changes back to olive black (5.0Y 3/2) again. The water content in unit 4 is varying occasionally between 31 and 53 % (Figure 15). At 88 cm depth, the water content is at its highest throughout the core, being 53 %. From this depth towards unit 5, the water content is decreasing.

The magnetic susceptibility is relatively stable in this unit, being approximately $20*10^{-5}$ SI (Figure 14).

The redness is more or less stable in unit 4, being 8-11 % (Figure 14). The lightness varies between 33-36 % (Figure 14). The graphs show notably higher and lower spectre of red and light at approximately 200 and 100 cm depth, but these are assumed to be measurement errors.

The percentages of total carbon, total organic carbon and calcium carbonate increase slightly towards the top of the unit (Figure 15). At the bottom of the unit, the percentage of total carbon is about 2.3. The total organic carbon is 1 %, and the calcium carbonate is 11 %. At approximately 50 cm depth, the total carbon decreases from 2.9 % to approximately 2.2 %, and calcium carbonate decreases from 13.8 % to approximately 9 %. The total organic carbon is about 1.2 % at the top.

Both the benthic and planktonic foraminiferal concentration are generally increasing towards the top of the unit (Figure 16). The benthic foraminiferal concentration varies between 93 no./g and 1718 no./g. The benthic foraminiferal concentration peaks at 50 cm depth (with 1718 no./g), The planktonic foraminiferal concentration is varying between 1 and 135 no./g. The benthic foraminiferal flux varies between approximately 2100 and 44 607 no./$cm^2k^{-1}$ (Figure 17). The planktonic foraminiferal flux is varying between 60 and 3943 no./$cm^2k^{-1}$ (Figure 17). The planktonic/benthic foraminiferal ratio is approximately 0 from the bottom of the core to 160 cm depth (Figure 16). Further up, the ratio varies between 0.03 and 0.13.

The number of IRD per gram sediment is approximately 0 (Figure 16). The IRD flux is low and stable (Figure 17). The flux is mainly varying from 0 to 9 no./$cm^2k^{-1}$, except at the bottom of the unit and at 190 cm depth, where the values are 31 and 21 no./$cm^2k^{-1}$.

## 5.5 Unit 5 (35-0 cm depth)

Unit 5 consist of clayey silt (Figure 11, Figure 15). The colouring of this unit is more or less homogeneous, being brownish black (2.5Y 3/1) (Figure 11). The water content in the lower part of unit 5 is approximately 37 % (Figure 15). Towards the most recent sediments, the water content is decreasing. As in unit 1, there are only a few sediment samples within unit 5, making the results limited.

The magnetic susceptibility is relatively stable in this unit, being approximately $20*10^{-5}$ SI (Figure 14). Except at approximately 35 cm depth, where the value is almost $40*10^{-5}$ SI.

The redness and lightness vary more in unit 5 compared to unit 4 (Figure 14). The redness varies between 8 and 11 %, while the lightness varies between 32-39 %. The redness and the lightness are peaking at approximately 25 and 11 cm depth, but the values are relatively low compared to the rest of the core. The XRF image does not reveal any pinkish layers in this unit (Figure 12).

The benthic foraminiferal concentration varies from approximately 250 to 540 no./g (Figure 16). The benthic foraminiferal flux varies between 4600 and 12 000 no./$cm^2k^{-1}$ (Figure 17). The planktonic foraminiferal concentration is relatively low within unit 6, being 5-16 no./g (Figure 16). The benthic foraminiferal flux varies from 90 to 400 no./$cm^2k^{-1}$ (Figure 17). The planktonic/benthic foraminiferal ratio is also relatively low, being 0.02-0.04 (Figure 16).

The number of IRD per gram sediment is approximately 1 (Figure 16), while the IRD flux is relatively high, varying from 8 to 31 no./$cm^2k^{-1}$ (Figure 17).

# 6 Interpretation and discussion

## 6.1 Construction of age model

The sedimentation rates between the calibrated radiocarbon dates are calculated to be 50.819 cm/ky (k=1000, y=year) (between 51.5 cm depth and 188 cm depth), 120.773 cm/ky (between 188 cm depth and 238 cm depth), and 37.801 cm/ky (between 238 cm depth and 414 cm depth).

Assuming that the sedimentation rates are the same outside of the given calibrated radiocarbon dates, the top of the core is estimated to be c. 6522 cal years BP. The till is found in unit 1 (476-445 cm depth). The age of the till is calculated to be >16 111 cal years BP, indicating the age of the sediments at the bottom of the core. The construction of the age model (Figure 18) is based on these datings and calculations.

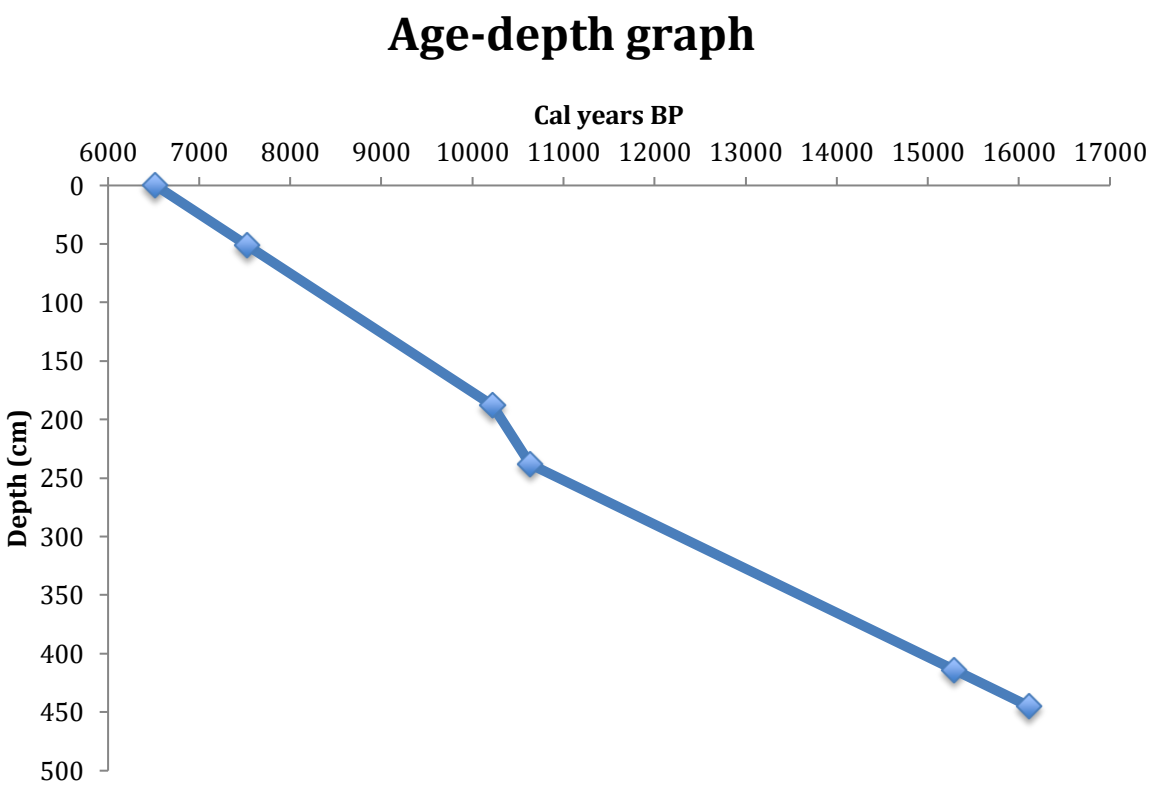


*Figure 18. Age-depth model based on the materials dated, and the estimated age of sediments outside the calibrated radiocarbon dates.*

The last 16 000 years can be divided into separate climate intervals: pre-Bølling interval, the Bølling-Allerød, the Younger Dryas and the Holocene. The glacial till implies that the pre-Bølling is > 16 100 cal years BP (> 445 cm depth). The Bølling-Allerød is interpreted to be from 16 100 to c. 13 000 cal years BP (445 – 325 cm depth) and the Younger Dryas from c. 13 000 to c. 12 000 cal years BP (325 – c. 300 cm depth). The transition from Younger Dryas to early Holocene is marked by rapid increase in IRD content at c. 300 cm depth, indicating an increase in iceberg and sea ice distribution. The Holocene is therefore c. <12 000 cal years BP (c. <300 cm depth). The most recent sediments are calculated to be c. 6500 cal years BP.

## 6.2 Magnetic susceptibility

The magnetic susceptibility of marine sediments is affected by changes in oceanography, glacial activity, provenance and grain size of sediments (Jessen et al., 2010). Highly magnetic material or non-magnetic material can be transported from its origin by ice rafting (Andrews and Tedesco, 1992; Grousset et al., 1993; Robinson et al., 1995; Stoner et al., 1996; Pirrung et al., 2002), mass transportation (Robinson et al., 2000; Kuijpers et al., 2001; Rasmussen et al., 2007) or melt water (Lekens et al., 2005; Rasmussen et al., 2007). Alteration in bottom currents and deep-water formation in the Nordic Seas influence the magnetic susceptibility in the North Atlantic and southern Norwegian Sea (Rasmussen et al., 1998; Kissel et al., 1997; Moros et al., 2002).

Sediments from the Last Glacial Maximum and the beginning of the deglaciation are characterized by higher and more variable magnetic susceptibility (Jessen et al., 2010). During the beginning of the early Holocene, the magnetic susceptibility increased (Jessen et al., 2010). Following that, the magnetic susceptibility gradually decreased towards the most present sediments (Jessen et al., 2010).

The magnetic susceptibility reaches its highest value in unit 1 (Figure 14). In unit 2, the magnetic susceptibility is low. The magnetic susceptibility is high and variable is in unit 3, while it is stable and low in unit 4 and 5. This indicates that the sediments in unit 1 and 3 are more magnetic compared to the rest.

## 6.3 Ice-rafted debris

As mentioned in the introduction “1.2 Ice-rafted debris (IRD)”, the quantity of IRD in marine sediments is equivalent to changes in iceberg distribution (Bond and Lotti 1995; Voelker et al., 2002).

In unit 2, 4 and 5, the amount of IRD is relatively low and stable (Figure 16 and Figure 17). In unit 1, the number of IRD per gram sediment reaches 16, which is the second highest value throughout the core (Figure 16). In unit 3, the concentration and flux are high and variable. The highest number of IRD per gram sediment is at c. 300 cm depth, being 41 no./g. The flux is measured to be 944 no./$cm^2k^{-1}$ (Figure 17). This indicates higher iceberg distribution in unit 1 and 3.

## 6.4 Pink layers

The spectre of red might indicate pink layers. Rasmussen and Thomsen (2013) stated that pink clay in marine sediments on Svalbard correlates to interstadials. They are transported by melt water, and are deposited during high surface temperatures and at high sedimentation rates (Rasmussen and Thomsen, 2013). Forwick et al. (2010) implied that reddish clay possibly could be transported by melt water run-off from retreating glaciers.

Due to the redness graph (Figure 14), the sediments are believed to be redder from approximately 405 to 250 cm depth. The highest spectre of red are found at 460 cm depth (unit 1), 430 cm depth (unit 2), 395-385 (unit 3), 380-360 cm depth (unit 3), 350-340 cm depth (unit 3), 315-310 cm depth (unit 3) and 290-260 cm depth (unit 3). The pink layers indicated by the redness graph are also visually found in the XRF images, except the one at 460 cm depth (Figure 12). The pink layers discovered are presented in Figure 19. A common denominator for these layers is that the magnetic susceptibility is either low or decreasing (Figure 19). The IRD content also decreases in these pink layers (Figure 19). Decreasing content of IRD suggest decreasing iceberg production and increasing melt water production. This strengthens the contention that pink sediments are correlating to interstadials (Rasmussen and Thomsen, 2013). The lightness follows the exact same pattern at the redness (Figure 19), indicating that the pink layers are corresponding with higher values of lightness.

The lightness of the sediment correlates to the amount of chalk (Hancock, 1984). Chalk findings in Arctic sediments are explained by ice rafting from areas south of 59°N, typically from the North Sea and the Baltic regions (e.g. Lehman, 1991; Hebbeln et al., 1994). During the Last Glacial Maximum and the deglaciation, these areas were covered by ice (e.g. Lehman, 1991).

Forwick et al. (2010) found that the pink sediments consisted of ankerite/dolomite, calcite, epidorite and phyllosilicates. Illite and mica were the most common phyllosilicates. Phyllosilicates give darker sediments, while ankerite/dolomite and calcite give lighter sediments (Forwick et al., 2010). High percentage of ankerite/dolomite and calcite may therefore explain the relationship between lightness and redness.

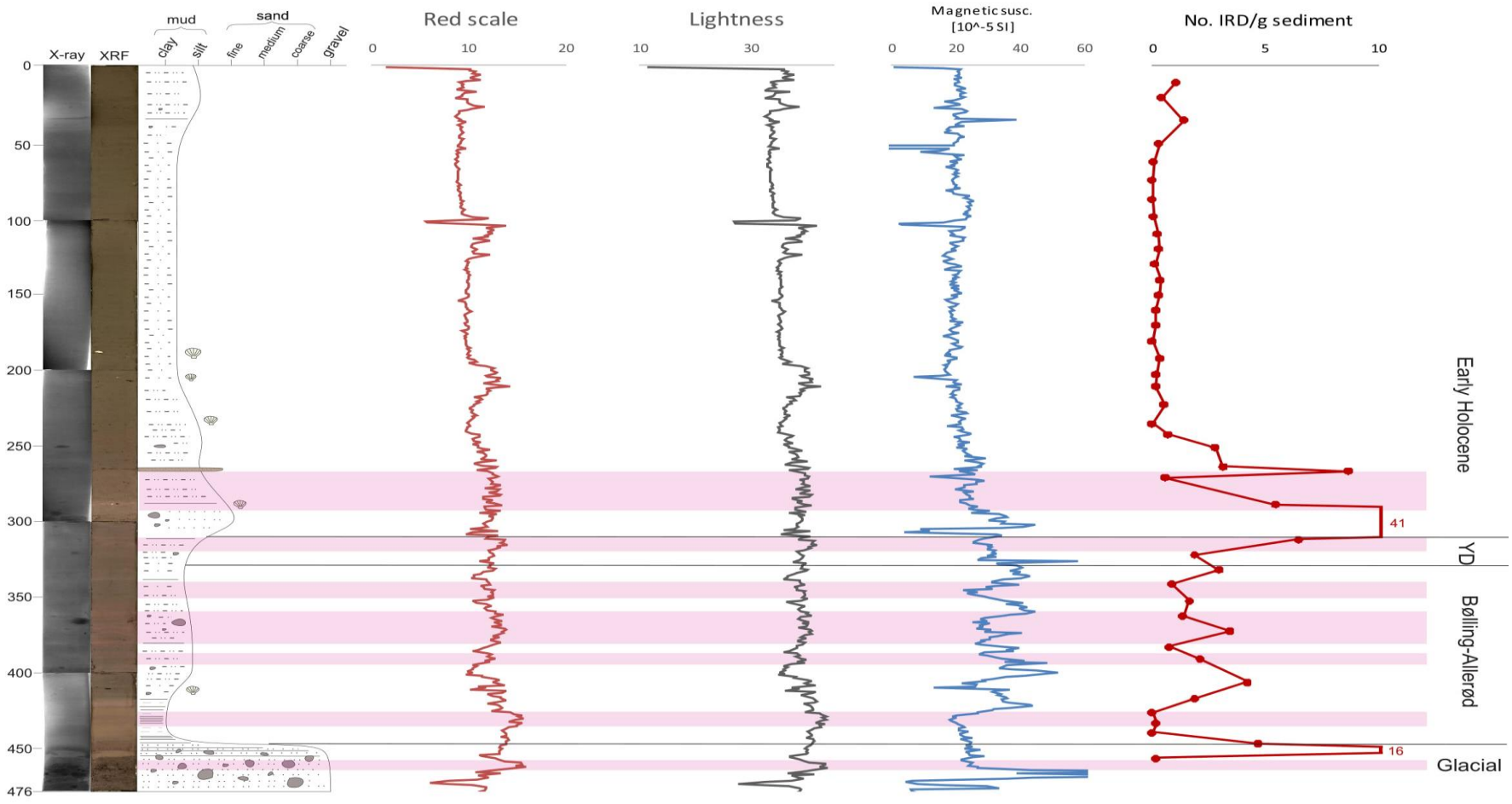


*Figure 19. Indication of the pink layers found in core HH18-1500GC. The pink layers, indicated by red scale and XRF images, are correlated with the lithological log, lightness, magnetic susceptibility and number of IRD per gram. The climate intervals are marked.*

## 6.5 Abundance of planktonic and benthic foraminifera

Low concentration and flux of planktonic foraminifera combined with high percentage of total organic carbon and low percentage of calcium carbonate are characteristic for cold conditions at the sea surface (Zamelczyk et al., 2014). Presence of Arctic surface water and seasonal sea ice correlates with cold conditions (Zamelczyk et al., 2012, 2013, 2014). During warmer conditions, the flux of planktonic foraminifera and the relative abundance of subpolar species are higher (Zamelczyk et al., 2014). Warmer conditions are often implied with a stronger advection of Atlantic water, which give a greater preservation of calcium carbonate (Zamelczyk et al., 2014). During cold conditions, the preservation of calcium carbonate shells is often poor (Heinrich, 1998; Huber et al., 2000).

The benthic foraminiferal concentration in core HH18-1500GC varies from 0 to approximately 1700 foraminifera per gram, while the planktonic foraminiferal concentration varies from 0 to approximately 135 foraminifera per gram (Figure 16). The concentrations of benthic and planktonic foraminifera follow similar trends, where the concentrations are greatest in the upper 150 cm of the core. The benthic foraminiferal flux increases from 0 at the bottom of the core to approximately 44 600 no./$cm^2k^{-1}$ at 50 cm depth, before it decreases (Figure 17). The planktonic foraminiferal flux follows the same pattern, reaching approximately 3500 no./$cm^2k^{-1}$ at 50 cm depth. The planktonic/benthic ratio foraminiferal is below 0 throughout the whole core, indicating that the conditions were in favour of benthic foraminifera (Figure 16). This is typical for shelf areas.

The total organic carbon is increasing gradually upwards in the core, except at approximately 300 and 100 cm depth (Figure 15). The percentage of total organic carbon is relatively high at approximately 445 cm depth, while calcium carbonate it low. The flux of planktonic and benthic foraminifera are extremely low at this depth. These results combined are characteristic for colder conditions at the sea surface. In unit 2, the calcium carbonate is relatively high, where the total organic carbon is low. The flux of planktonic and benthic foraminifera is, on the other hand, low in this unit (Figure 17). At 300 cm depth, the percentage of calcium carbonate is at its highest. The flux of planktonic and benthic foraminifera show a rapid increase at this point (Figure 17), indicating warmer conditions. Presence of Arctic surface water may be discovered in unit 5. The total carbon percentage is

at its highest, while the calcium carbonate is notably low. The flux of benthic and planktonic foraminifera are also decreasing.

## 6.6 Regional perspective

Slubowska-Woldengen et al. (2008) studied past ocean circulation changes on the continental shelves in the Nordic and Barents Seas. This was done collecting data from 12 studies. Figure 20 (Slubowska-Woldengen et al., 2008) illustrates the different study sites. In this paper, the last 16 000 cal years BP was divided into five sections: the late glacial (16 000-15 000 cal years BP), the Bølling-Allerød (14 500-13 500 cal years BP), the Younger Dryas (12 500-11 500 cal years BP), the early Holocene (9500-7500 cal years BP) and the late Holocene (4000-2000 cal years BP).

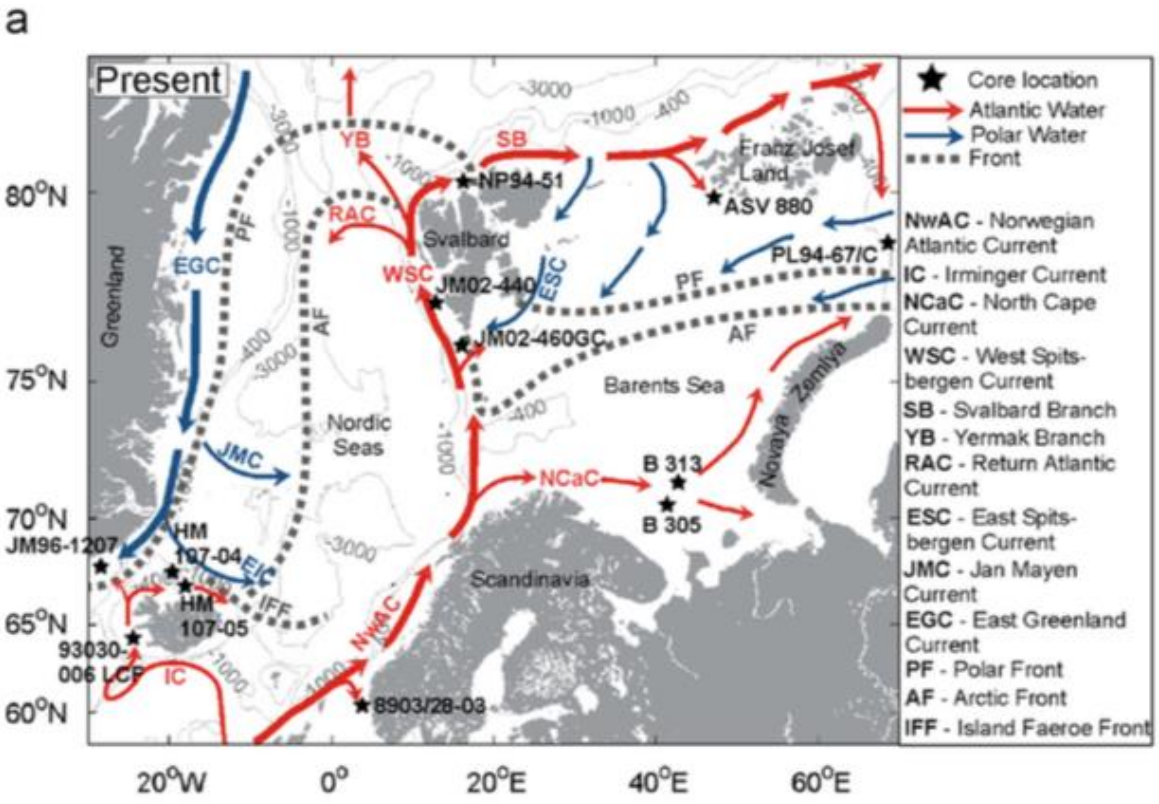


*Figure 20. Location map of all the core sites used in Slubowska-Woldengen et al. (2008).*

Comparing the results presented in Slubowska-Woldengen et al. (2008) with the results from HH18-1500GC, the focus will be on the data from HM107-05, 8903/28-03, B 305, JM02-460GC, JM02-440 (Slubowska-Woldengen et al., 2007) and NP94-51 (Slubowska et al., 2005). Core HM107-05 was retrieved north of Iceland, 8903/28-03 from the northern North Sea, B 305 from the southeastern part of the Barents Sea, JM02-460GC from southern Svalbard, JM02-440 from western Svalbard, and NP94-51 from northern Svalbard (Hinlopen). The different benthic foraminiferal species have not been identified in core

HH18-1500GC. Even though, the results concerning the relative abundance of benthic foraminifera and IRD content in Slubowska-Woldengen et al. (2008) can be used to determine some of the previous ocean conditions in the Hinlopen Trough.

In the late glacial, the relative abundance of the benthic foraminiferal species *E. excavaturn* and *C. reniforme* was high in the northern North Sea, on northern Svalbard/Hinlopen and western Svalbard, indicating cold conditions with relatively fresh water, and presence of Arctic water (Slubowska-Woldengen et al., 2008). The abundance of *C. neoteretis* was 47 % on northern Iceland (Knudsen et al., 2004). High abundance of *C. neoteretis* corresponds to saline, cool Atlantic water (e.g. Wollenburg et al., 2004).

During the Bølling-Allerød interstadial, the abundance of *C. neoteretis* and *C. reniforme* was high in the northern North Sea and around Svalbard (Slubowska et al., 2005; Slubowska-Woldengen et al., 2007). This combination of species indicates an intrusion of saline, cool Atlantic water, and a transformation from polar to subarctic conditions (Slubowska-Woldengen et al., 2008). In the southeastern part of the Barents Sea, *I. norcrossi* and *E. excavatum* dominated (Polyak and Mikhailov, 1996), which implies polar conditions (Slubowska-Woldengen et al., 2008). Polar conditions were also found on northern Iceland (Knudsen et al., 2004).

Due to the relative abundance of the different species, the conditions during the Younger Dryas were polar in the northern North Sea, around Svalbard, and the southeastern Barents Sea (Slubowska-Woldengen et al., 2008). High IRD concentrations north of Iceland, in the northern North Sea and south of Svalbard support a polar climate with higher distribution of sea ice and/or icebergs (Slubowska-Woldengen et al., 2008). The concentration of IRD in HH18-1500GC was increasing during the Younger Dryas (Figure 22), which correlates to the results seen in Slubowska-Woldengen et al. (2008).

In the early Holocene, the abundance of *E. excavatum* was relatively low (0-10 %) in all cores. *C. reniforme* and *N. labradorica* dominate around Svalbard (Slubowska-Woldengen et al., 2007). As mentioned before, C. reniforme indicates strong advection of cool, saline Atlantic water. High abundance of *N. labradorica* indicates proximity of the Arctic and the Polar Front proximity (Slubowska-Woldengen et al., 2006). In the southeastern Barents Sea and northern Iceland, *M. barleeanum* dominated, which indicate high salinity waters and

strong biological production (e.g. Hald and Steinsund, 1996). *M. barleeanum* also implies a stronger advection of Atlantic water (Slubowska-Woldengen et al., 2008). The amount of IRD in the whole study area was low during the early Holocene (Slubowska-Woldengen et al., 2008), correlating to the IRD content of HH18-1500GC during the early Holocene (Figure 22).

In the late Holocene, the diversity among the benthic foraminifera was higher compared to the previous climate intervals. Around Svalbard, the abundance of *E. excavatum* increases (JM02-460GC, JM02-440, NP94-51) together with the abundance of *C. reniforme* (JM02-460GC, JM02-440). As seen in the last glacial, the combination of these foraminifera indicate colder conditions with relatively fresh water, and presence of Arctic water. The top sediments of HH18-1500GC are calculated to be c. 6500 cal years BP, indicating that the core is not consisting of sediments from the late Holocene.

Core NP94-51 was retrieved close to HH18-1500GC, outside the mouth of the Hinlopen Strait, at 80.21.411 °N and 16.17.942 °E (Figure 20; Slubowska-Woldengen et al., 2008) (Slubowska et al., 2005). The core length was approximately 7 m. NP94-51 did not contain any till, making it hard to determine the timing of the retreat of the ice sheet. Slubowska et al. (2005) interpreted that in the glacial and deglacial interval (17 000 to 11 000 cal years BP), the abundance of planktonic and benthic foraminifera were very low, which indicate low biological productivity. During the early and the mid Holocene, the number of IRD was low, while the abundance of planktonic and benthic foraminifera are relatively high (Slubowska et al., 2005). They stated that these parameters implied no or very few icebergs during this period, together with conditions in favour of benthic foraminifera (Slubowska et al., 2005). These results are illustrated in Figure 21 (Slubowska et al, 2005). Slubowska et al. (2005) are using an old calibration method, meaning that the new calibration methods applied in core HH18-1500GC might not correlate to the old method.

Comparing the results from HH18-1500GC (Figure 22) with the results in Slubowska et al. (2005) (Figure 21), a predominant difference is that HH18-1500GC reaches into till, while NP94-51 does not. Both cores are taken from Hinlopen, and the age of the till in HH18-1500GC indicate when the ice retreated from the area. The age of the till is calculated to be c. 16 100 cal years BP. The top of the core HH18-1500GC is estimated to be c. 6500 cal years

BP, while NP94-51 contains sediments from late Holocene. The core HH18-1500GC was taken at the edge of the trough in order to be certain to reach into till, therefore in the last 7000 there can have been erosion or non-deposition from stronger bottom current activities.

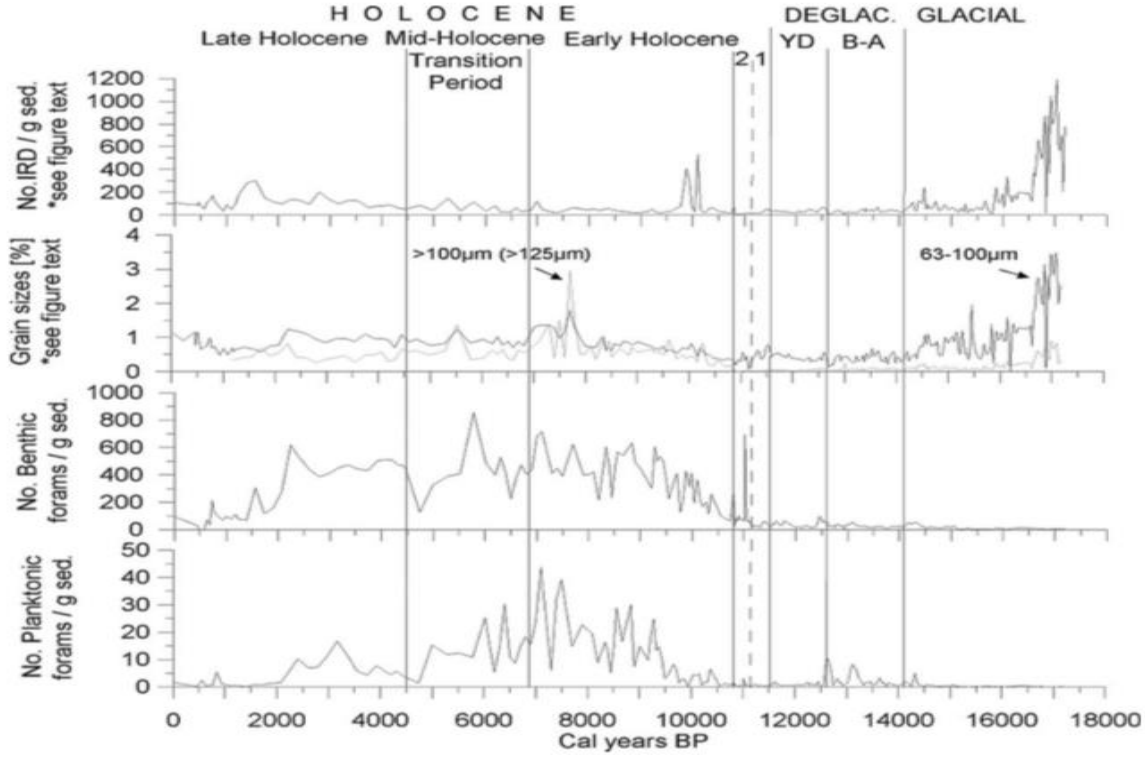


*Figure 21. This figure provided data from Slubowska et al. (2005). The number of planktonic foraminifera per gram (concentration of planktonic foraminifera), the number of benthic foraminifera per gram (concentration of benthic foraminifera) and number of IRD per gram versus the interpreted calibrated years BP and the geological periods. YD is an abbreviation for the Younger Dryas stadial. B-A means the Bølling-Allerød interstadial. 1 and 2 indicates the first and second step of the alteration between Younger Dryas and the Holocene.*

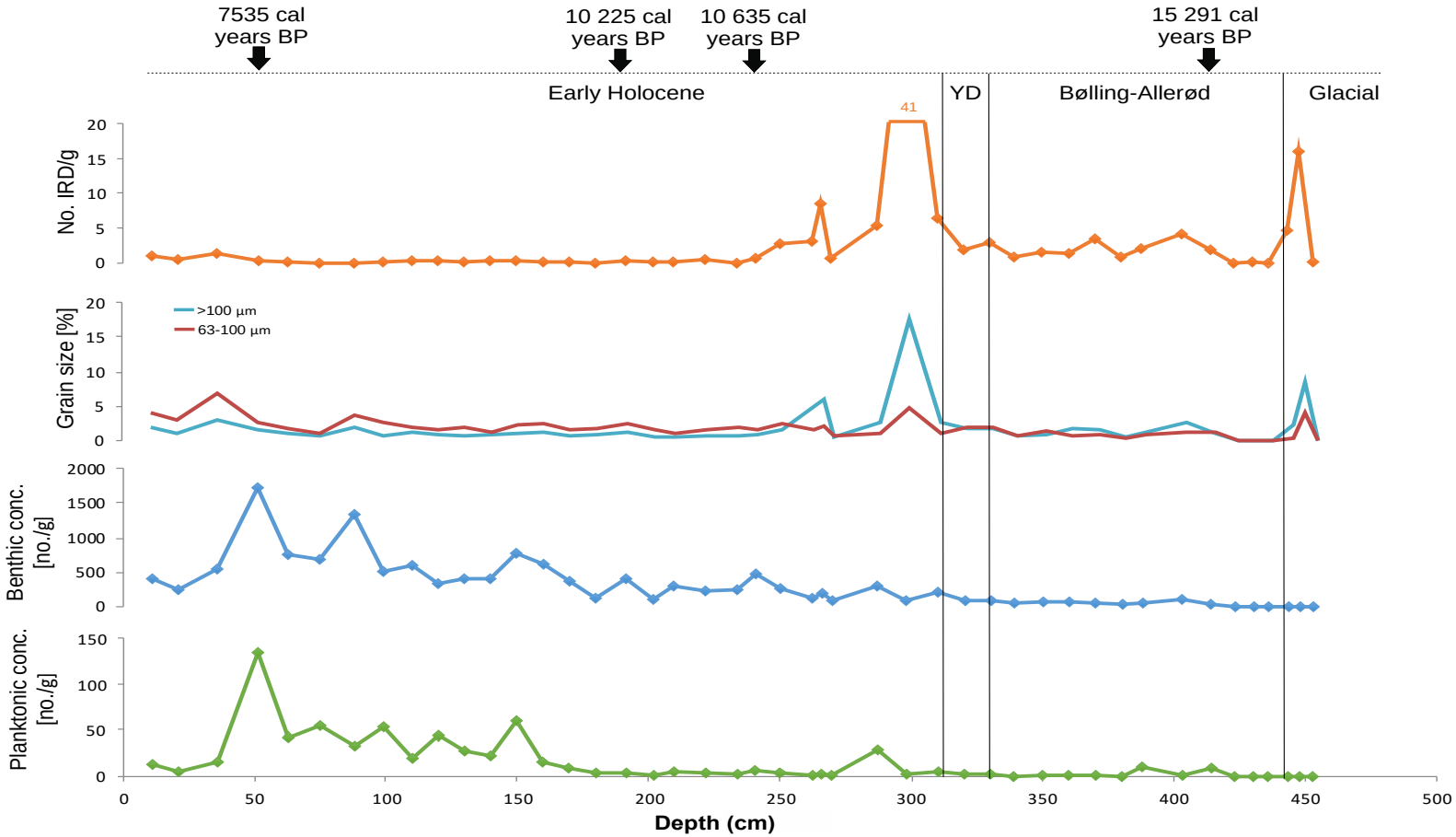


*Figure 22. This figure shows the concentrations of planktonic foraminifera (green graph) and benthic foraminifera (blue graph), and the number of IRD per gram sediment (orange graph) together with the grain size distribution changing with depth in core HH18-1500GC. The calibrated radiocarbon datings at 51.5 cm, 188 cm, 238 cm and 414 cm depth are indicated with stippled lines.*

Nielsen and Rasmussen (2018) studied gravity core HH12-1212GC (Figure 23; Nielsen and Rasmussen, 2018) retrieved from Storfjorden in southern Svalbard. They interpreted that the core consisted of glacial till, sediments from the Bølling interstadial (c. 15 600 to 15 300 cal years BP), the Allerød interstadial (<14 500 cal years BP), Younger Dryas and the Holocene (<11 700 cal years BP) (Rasmussen and Thomsen, 2015). The lithological log of HH12-1212GC is presented with number of IRD per gram, benthic foraminiferal concentration and calibrated age (Figure 23; Nielsen and Rasmussen, 2018). This record was calibrated with an updated program, and the timing is therefore slightly different from Slubowska et al. (2005) and Slubowska-Woldengen et al. (2007, 2008).

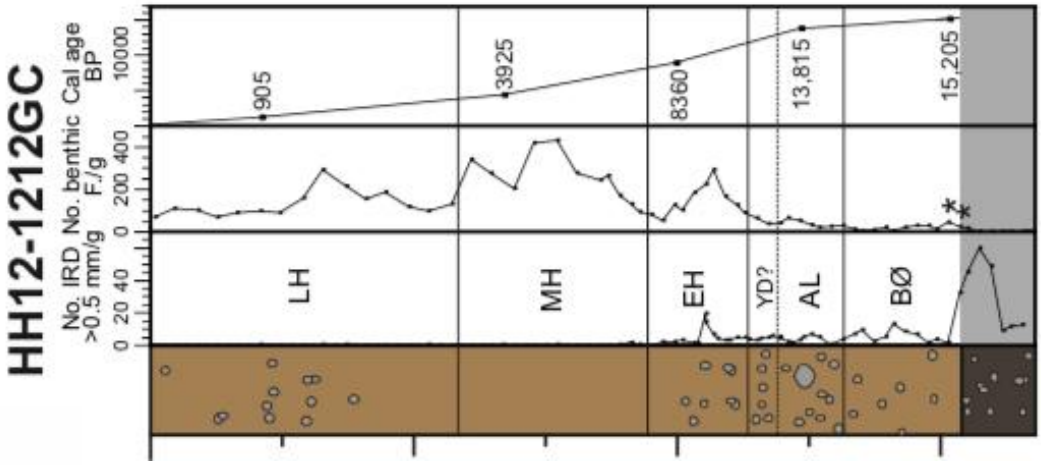


*Figure 23. The lithological log of core HH12-1212GC combined with the number of IRD per gram (>0.5 mm) and the number of benthic foraminifera per gram versus the calibrated years BP and the geological periods. BØ is an abbreviation for Bølling, AL is for Allerød, YD is for Younger Dryas, EH is for the early Holocene, MH is for the mid Holocene and LH is for the late Holocene. The grey bars indicate the glacial till (Nielsen and Rasmussen, 2018).*

Since Nielsen and Rasmussen (2018) results are based on the new calibration program, it is more expected to compare well to the results from HH18-1500GC (Figure 22). However, the start of Bølling interstadial in HH12-1212GC is dated to c. 15 300 cal years BP (Nielsen and Rasmussen, 2018). The IRD concentration in HH12-1212GC was at its highest in the pre-Bølling interval (Figure 23; Nielsen and Rasmussen, 2018). This correlates with the peak in the glacial till at c. 450 cm depth in HH18-1500GC (Figure 22). The age of this peak is calculated to be c. 16 100 cal years BP, implying that the Bølling-Allerød interval in Hinlopen dates older than in Storfjorden. The cause for this is probably differences in reservoir ages between the two areas – the northern Svalbard margin at the edge of the Arctic Ocean is expected to have increased reservoir ages compared to the southern position of HH12-

1212GC directly affected by strong flow of Atlantic Water. The benthic foraminiferal concentrations of HH18-1500GC and HH12-1212GC were low within Bølling-Allerød interval. From the beginning of the early Holocene and in the mid Holocene, the benthic foraminiferal concentration of HH12-1212GC was relatively high and variable (Figure 23; Nielsen and Rasmussen, 2018). This is also indicated in NP94-51 (Figure 21; Slubowska et al., 2005) and HH18-1500GC (Figure 22).

Slubowska-Woldengen et al. (2007) studied the gravity core JM02-440GC that was retrieved in the Bellsund Trough, western Svalbard (Figure 20; Slubowska-Woldengen et al., 2008). Slubowska-Woldengen at al. (2007) has used the same calibration program as Slubowska et al. (2005) due to lack of data on reservoir age differences between the two localities. Slubowska-Woldengen et al. (2007) have been looking at the flux of IRD, and the flux of benthic and planktonic foraminifera (Figure 24; Slubowska-Woldengen et al., 2007).

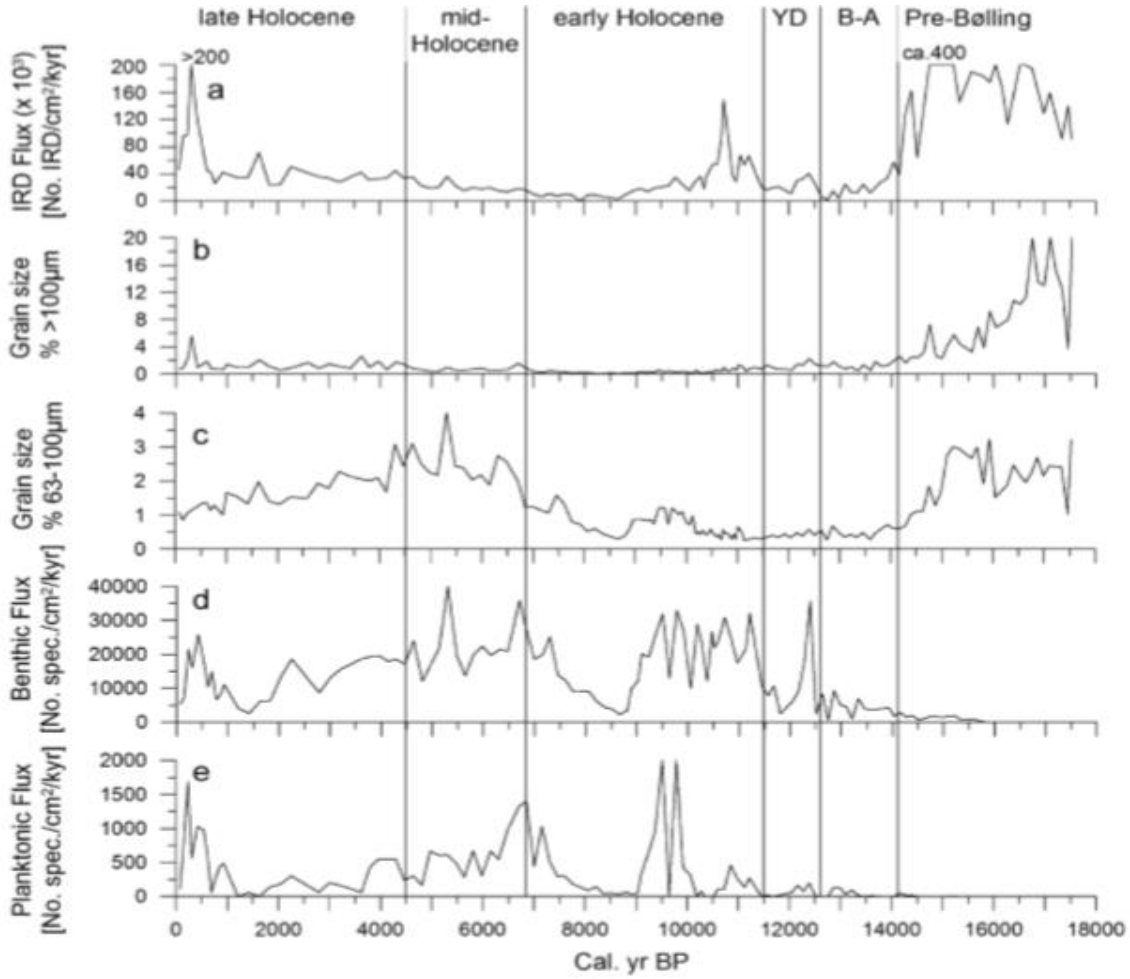


*Figure 24. This figure provides data from Slubowska-Woldengen et al. (2007). The planktonic foraminiferal flux (e), the benthic foraminiferal flux (d) and the IRD flux (a) versus the interpreted calibrated years BP and the geological periods. The abbreviations are the same as in figure 16.*

Slubowska-Woldengen et al. (2007) found that the flux of IRD was highest during the pre-Bølling, together with exceptionally low flux of planktonic and benthic foraminifera. These parameters correlate to cold conditions on the ocean floor and sea ice cover (Slubowska-Woldengen et al., 2007). The IRD flux decreased in the Bølling-Allerød interval. During the Younger Dryas, the IRD flux increased slightly. The benthic foraminiferal flux peaked, while the planktonic foraminiferal flux was low. In the beginning of the early Holocene, the IRD flux peaked. The benthic foraminiferal flux was relatively high, and showed large variations. The planktonic foraminiferal flux was at its highest, with a value of 2000 number of species per square centimetre per thousand years, at c. 9000-10 000 cal years BP. At c. 7000 years BP, both the planktonic and benthic foraminiferal flux were relatively high. High flux of benthic and planktonic foraminifera imply warmer conditions, with influence of Atlantic water.

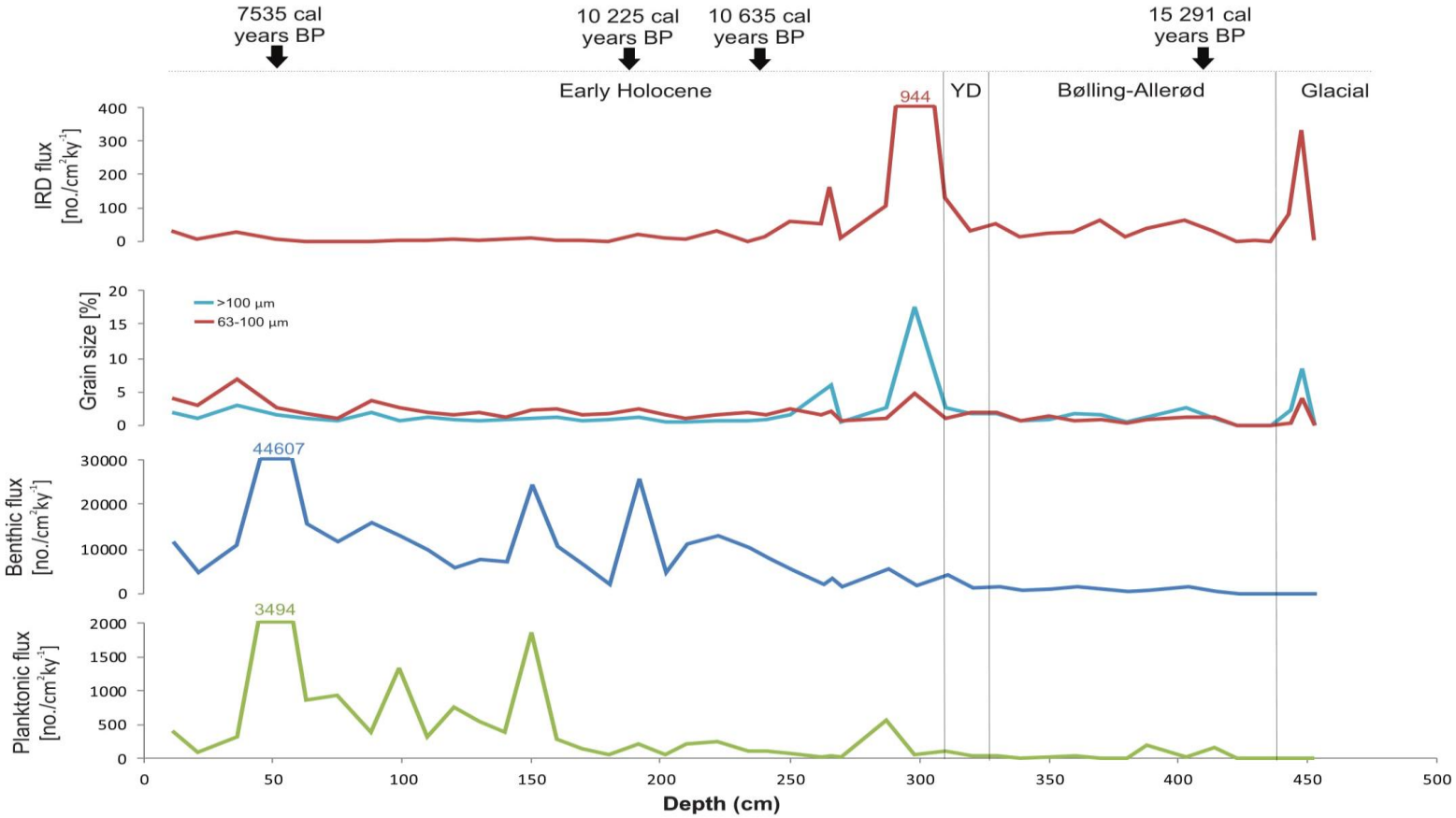


*Figure 25. This figure shows the planktonic foraminiferal flux, the benthic foraminiferal flux and the IRD flux combined with the grain size distribution varying with depth in core HH18-1500GC. The calibrated radiocarbon datings at 51.5 cm, 188 cm, 238 cm and 414 cm depth are indicated with stippled lines.*

At c. 300 cm depth in HH18-1500GC, the IRD flux peaks, the foraminiferal fluxes slightly increase, and the grain size distribution show higher percentage of particles above 100 μm (Figure 25). Using the age-depth model (Figure 18), the estimated age at 300 cm is c. 12 275 cal years BP. Due to JM02-440 (Figure 24; Slubowska-Woldengen et al., 2007) this is within the Younger Dryas stadial. Thus, the foraminiferal fluxes are slightly increasing at this depth (Figure 25); the sediments at 300 cm depth in HH18-1500GC are therefore believed to be of the beginning of the early Holocene. In the beginning of Holocene, there was an inflow of more saline and cold Atlantic water, which made the biological productivity stronger (Slubowska et al., 2005). The ice retreated and sea ice melted, causing increased melt water run-off, providing higher IRD fluxes. The characteristics of HH18-1500GC at 300 cm depth (Figure 25), correlating to the peak of benthic foraminiferal concentration and IRD content in HH12-1212GC in the early Holocene (Figure 23; Nielsen and Rasmussen, 2018). In HH18-1500GC the planktonic foraminiferal flux peaks at c. 150 cm depth, combined with a high benthic foraminiferal flux (Figure 25). Using the age-depth model (Figure 18), the estimated age at 150 cm depth is c. 9500 cal years BP. The highest planktonic foraminiferal flux in JM02-440 was also c. 9500 cal years BP, combined with a notably high benthic foraminiferal flux (Figure 24; Slubowska-Woldengen et al., 2007). At 7500 cal years BP the foraminiferal fluxes peak in both cores. These peaks indicate events with warmer conditions where the advection of Atlantic water is stronger (Zamelczyk et al., 2014).

## 6.7 Interpretation

The till in unit 1 is estimated to be >16 100 cal years BP. This indicates that the sediments below 445 cm depth are glacial. The high magnetic susceptibility (Figure 14) in unit 1 supports this interpretation (Jessen et al., 2010). Thus, the percentage of total organic carbon is relatively high, combined with low percentage of calcium carbonate and foraminiferal fluxes indicate Arctic conditions (Zamelczyk et al., 2012, 2013, 2014) and poor biological productivity (Slubowska et al., 2005).

The magnetic susceptibility is varying extremely from higher to lower values from approximately 445 cm depth to approximately 300 cm depth (Figure 14), which is common for sediments from the deglaciation (Jessen et al., 2010). Due to this, the deglaciation is interpreted to be c. 16 100 – c. 12 000 cal years BP. The deglaciation can be divided into the Bølling-Allerød and the Younger Dryas (Jessen et al., 2010).

The first inflow of Atlantic water after the Last Glacial Maximun was during the Bølling-Allerød interstadial (Slubowska et al., 2005). The interval is just above the till, meaning that the start of the Bølling-Allerød is dated to be c. 16 100 cal years BP. During the Bølling-Allerød, the number of IRD per gram and the IRD flux of HH18-1500GC (Figure 22 and Figure 25). This is seen in several studies (Slubowska et al., 2005; Slubowska-Woldengen et al, 2007; Nielsen and Rasmussen, 2018).

At approximately 325 cm depth, the flux of IRD and benthic foraminifera slightly increase (Figure 25), indicating the transitioning to the Younger Dryas stadial (e.g. Slubowska-Woldengen et al., 2007). At 325 cm depth, the age of HH18-1500 is c. 13 000 cal years BP.

The deglaciation contains five distinctive pink layers (Figure 20). Pink layers are correlating to warmer conditions, when ice melts back and run-off of turbid meltwater is high (Rasmussen and Thomsen, 2013). The presence of pink layers is mostly within the Bølling-Allerød interval (Figure 20), indicating at least five interstadial-stadial events.

The transitioning to the early Holocene is indicated by the rapid increase in IRD flux at c. 12 000 cal years BP (c. 300 cm depth) (Figure 25). The magnetic susceptibility is stable with small variations (Figure 14). The amount of IRD per gram decreases after the rapid increase at approximately 300 cm depth (Figure 22). The planktonic and benthic foraminiferal

concentrations and flux increase towards 50 cm depth (Figure 22 and Figure 23), implying stronger advection of Atlantic water. The upper 240 cm of the core consists of mainly clay (Figure 11, Figure 15), except from unit 5 where the sediments are of clayey silt. This indicates stronger ocean currents. From c. 7500 cal years BP (c. 50 cm depth), the foraminiferal and IRD flux decrease (Figure 25). This may indicate a transformation concerning colder conditions. The most recent sediments in HH18-1500GC are calculated to be 6522 cal years BP, implying that the core does not contain sediments from the late Holocene, due to erosion or non-deposition from stronger bottom current activities.

The core consists of mainly fine-grained sediments (Figure 11, Figure 15), except from section below c. 445 cm depth. Therefore, it is reason to believe that the upper 445 cm of the core was deposited under undisturbed circumstances.

# 7 Conclusion

The sediment core HH18-1500GC retrieved in the Hinlopen Trough, northern Svalbard, has been investigated to reconstruct the climatic evolution and ocean circulation over the last 16 000 years. Climatic changes occurring on the western and northern margins of Svalbard may affect the whole Artic, making it a particularly interesting area of study. The core was taken at the shelf edge of the trough in order to be certain to reach into till, with intent of dating the retreat of the ice sheet.

- The retreat of the ice sheet was dated c. 16 100 cal years BP in the Hinlopen Trough, northern Svalbard. The glacial sediments revealed Arctic conditions with low biological productivity.
- The deglaciation occurred from c. 16 100 cal years BP to c. 12 000 cal years BP. Sediments from the Bølling-Allerød interstadials (c. 16 100 – 13 000 cal years BP) and the Younger Dryas stadials (c. 13 000 – 12 000 cal years BP) were found. Pink sediments are discovered in distinct layers deposited mostly during the Bølling-Allerød interval. The pink layers are correlated to decreasing magnetic susceptibility and IRD content, characteristic for warmer conditions. These layers indicate at least five interstadial-stadial events, commonly known as Dansgaard-Oeschger (DO) event (Dansgaard et al., 1984).
- The early Holocene began c. 12 000 cal years BP presented by increasing IRD and foraminiferal content, implying retreating ice sheet and melting of sea ice, causing increased melt water run-off. The conditions during the early Holocene were in favour of benthic foraminifera; implied by presence of Atlantic water. Approximately 7500 cal years BP, there is interpreted a transition towards polar conditions as the foraminiferal fluxes decreased and the IRD flux increased. The most recent sediments are c. 6500 cal years BP, indicating erosion or non-deposition due to strong bottom currents activity on the shelf edge.

# 8 Appendices

## 8.1 Appendix 1

| Depth (cm) | Dry weight (g) | Sample fraction (Splits) | Counted squares | Benthic total | Planktic total | Benthic estimation | Benthic concentration (forams/g) | Planktic estimation | Planktic concentration (forams/g) | Planktic/Benthic ratio |
|---|---|---|---|---|---|---|---|---|---|---|
| 11 | 22,97 | 2 | 4 | 203 | 7 | 9135,00 | 397,69 | 315,00 | 13,71 | 0,0345 |
| 21 | 14,54 | 2 | 10 | 200 | 4 | 3600,00 | 247,59 | 72,00 | 4,95 | 0,0200 |
| 36 | 15,86 | 2 | 5 | 238 | 7 | 8568,00 | 540,23 | 252,00 | 15,89 | 0,0294 |
| 51,5 | 20,06 | 2 | 2 | 383 | 30 | 34470,00 | 1718,34 | 2700,00 | 134,60 | 0,0783 |
| 63 | 15,63 | 2 | 3 | 200 | 11 | 12000,00 | 767,75 | 660,00 | 42,23 | 0,0550 |
| 75 | 13,08 | 2 | 4 | 201 | 16 | 9045,00 | 691,51 | 720,00 | 55,05 | 0,0796 |
| 88 | 9,15 | 2 | 3 | 204 | 5 | 12240,00 | 1337,70 | 300,00 | 32,79 | 0,0245 |
| 99 | 19,67 | 1 | 2 | 225 | 23 | 10125,00 | 514,74 | 1035,00 | 52,62 | 0,1022 |
| 110 | 12,67 | 2 | 5 | 211 | 7 | 7596,00 | 599,53 | 252,00 | 19,89 | 0,0332 |
| 120 | 13,43 | 2 | 8 | 202 | 26 | 4545,00 | 338,42 | 585,00 | 43,56 | 0,1287 |
| 130 | 15,15 | 1 | 3 | 202 | 14 | 6060,00 | 400,00 | 420,00 | 27,72 | 0,0693 |
| 140 | 14,17 | 2 | 7 | 220 | 12 | 5657,14 | 399,23 | 308,57 | 21,78 | 0,0545 |
| 150 | 24,23 | 2 | 2 | 210 | 16 | 18900,00 | 780,02 | 1440,00 | 59,43 | 0,0762 |
| 160 | 13,54 | 2 | 5 | 229 | 6 | 8244,00 | 608,86 | 216,00 | 15,95 | 0,0262 |
| 170 | 13,07 | 2 | 8 | 219 | 5 | 4927,50 | 377,01 | 112,50 | 8,61 | 0,0228 |
| 180 | 13,9 | 0 | 6 | 219 | 6 | 1642,50 | 118,17 | 45,00 | 3,24 | 0,0274 |
| 191,5 | 21,07 | 2 | 5 | 233 | 2 | 8388,00 | 398,10 | 72,00 | 3,42 | 0,0086 |
| 202 | 16,91 | 0 | 7 | 245 | 3 | 1575,00 | 93,14 | 19,29 | 1,14 | 0,0122 |
| 210 | 12,74 | 2 | 10 | 204 | 4 | 3672,00 | 288,23 | 72,00 | 5,65 | 0,0196 |
| 222 | 18,93 | 2 | 9 | 213 | 4 | 4260,00 | 225,04 | 80,00 | 4,23 | 0,0188 |
| 234 | 13,86 | 2 | 11 | 205 | 2 | 3354,55 | 242,03 | 32,73 | 2,36 | 0,0098 |
| 241 | 17,4 | 2 | 5 | 231 | 3 | 8316,00 | 477,93 | 108,00 | 6,21 | 0,0130 |
| 250 | 21,92 | 2 | 7 | 217 | 3 | 5580,00 | 254,56 | 77,14 | 3,52 | 0,0138 |
| 262 | 16,94 | 2 | 18 | 206 | 2 | 2060,00 | 121,61 | 20,00 | 1,18 | 0,0097 |
| 265,6 | 19,61 | 2 | 10 | 203 | 2 | 3654,00 | 186,33 | 36,00 | 1,84 | 0,0099 |
| 269,5 | 17,51 | 1 | 13 | 213 | 3 | 1474,62 | 84,22 | 20,77 | 1,19 | 0,0141 |
| 287 | 20,11 | 2 | 7 | 227 | 23 | 5837,14 | 290,26 | 591,43 | 29,41 | 0,1013 |
| 298 | 23,88 | 3 | 45 | 228 | 8 | 1824,00 | 76,38 | 64,00 | 2,68 | 0,0351 |
| 310 | 21,01 | 2 | 9 | 222 | 6 | 4440,00 | 211,33 | 120,00 | 5,71 | 0,0270 |
| 320 | 17,76 | 2 | 27 | 199 | 5 | 1326,67 | 74,70 | 33,33 | 1,88 | 0,0251 |
| 330 | 18,33 | 2 | 24 | 226 | 6 | 1695,00 | 92,47 | 45,00 | 2,45 | 0,0265 |
| 339 | 16,09 | 1 | 26 | 205 | 2 | 709,62 | 44,10 | 6,92 | 0,43 | 0,0098 |
| 350 | 15,42 | 1 | 18 | 202 | 3 | 1010,00 | 65,50 | 15,00 | 0,97 | 0,0149 |
| 360 | 22,05 | 1 | 12 | 214 | 4 | 1605,00 | 72,79 | 30,00 | 1,36 | 0,0187 |
| 370 | 19,45 | 2 | 37 | 212 | 2 | 1031,35 | 53,03 | 9,73 | 0,50 | 0,0094 |
| 380 | 18,76 | 0 | 18 | 243 | 3 | 607,50 | 32,38 | 7,50 | 0,40 | 0,0123 |
| 388 | 18,92 | 1 | 21 | 198 | 47 | 848,57 | 44,85 | 201,43 | 10,65 | 0,2374 |
| 403 | 15,65 | 2 | 24 | 205 | 2 | 1537,50 | 98,24 | 15,00 | 0,96 | 0,0098 |
| 414 | 16,97 | 1 | 31 | 205 | 56 | 595,16 | 35,07 | 162,58 | 9,58 | 0,2732 |
| 423 | 17,09 | 0 | 45 | 0 | 0 | 0,00 | 0,00 | 0,00 | 0,00 | #DIV/0! |
| 430 | 16,4 | 0 | 45 | 0 | 1 | 0,00 | 0,00 | 1,00 | 0,06 | #DIV/0! |
| 436 | 15,41 | 0 | 45 | 0 | 0 | 0,00 | 0,00 | 0,00 | 0,00 | #DIV/0! |
| 443,5 | 18,33 | 0 | 45 | 6 | 0 | 6,00 | 0,33 | 0,00 | 0,00 | 0,0000 |
| 448 | 21,79 | 0 | 45 | 0 | 0 | 0,00 | 0,00 | 0,00 | 0,00 | #DIV/0! |
| 453 | 15,89 | 0 | 45 | 7 | 0 | 7,00 | 0,44 | 0,00 | 0,00 | 0,0000 |

## 8.3 Appendix 2

| Depth (cm) | Dry weight (g) | IRD counted | No. IRD/g |
|---|---|---|---|
| 11 | 22,97 | 24 | 1,04 |
| 21 | 14,54 | 6 | 0,41 |
| 36 | 15,86 | 22 | 1,39 |
| 51,5 | 20,06 | 6 | 0,30 |
| 63 | 15,63 | 1 | 0,06 |
| 75 | 13,08 | 0 | 0,00 |
| 88 | 9,15 | 0 | 0,00 |
| 99 | 19,67 | 1 | 0,05 |
| 110 | 12,67 | 3 | 0,24 |
| 120 | 13,43 | 4 | 0,30 |
| 130 | 15,15 | 2 | 0,13 |
| 140 | 14,17 | 5 | 0,35 |
| 150 | 24,23 | 7 | 0,29 |
| 160 | 13,54 | 2 | 0,15 |
| 170 | 13,07 | 2 | 0,15 |
| 180 | 13,9 | 0 | 0,00 |
| 191,5 | 21,07 | 7 | 0,33 |
| 202 | 16,91 | 3 | 0,18 |
| 210 | 12,74 | 2 | 0,16 |
| 222 | 18,93 | 10 | 0,53 |
| 234 | 13,86 | 0 | 0,00 |
| 241 | 17,4 | 12 | 0,69 |
| 250 | 21,92 | 61 | 2,78 |
| 262 | 16,94 | 53 | 3,13 |
| 265,6 | 19,61 | 170 | 8,67 |
| 269,5 | 17,51 | 10 | 0,57 |
| 287 | 20,11 | 109 | 5,42 |
| 298 | 23,88 | 981 | 41,08 |
| 310 | 21,01 | 136 | 6,47 |
| 320 | 17,76 | 33 | 1,86 |
| 330 | 18,33 | 54 | 2,95 |
| 339 | 16,09 | 14 | 0,87 |
| 350 | 15,42 | 25 | 1,62 |
| 360 | 22,05 | 30 | 1,36 |
| 370 | 19,45 | 67 | 3,44 |
| 380 | 18,76 | 14 | 0,75 |
| 388 | 18,92 | 40 | 2,11 |
| 403 | 15,65 | 66 | 4,22 |
| 414 | 16,97 | 32 | 1,89 |
| 423 | 17,09 | 0 | 0,00 |
| 430 | 16,4 | 3 | 0,18 |
| 436 | 15,41 | 0 | 0,00 |
| 443,5 | 18,33 | 86 | 4,69 |
| 448 | 21,79 | 347 | 15,92 |
| 453 | 15,89 | 3 | 0,19 |

# 8.4 Appendix 3

| Depth (cm) | Wet weight (g) | Dry weight (g) | Volume sediment sample (cm3) | Porosity (g/cm3) | Wet Bulk Density (g/cm3) | Dry Bulk Density (g/cm3) | Sedimentation rate (cm/y) | Linear Sedimentation Rate (cm/ky) | Mass Accumulation Rate (g/((cm)^2*(ky)^-1)) | Benthic conc. (forams/g) | Benthic flux (no./((cm)^2*(ky)^-1)) | Planktonic conc. (forams/g) | Planktonic flux (no./((cm)^2*(ky)^-1)) | No. IRD/g | IRD flux (no./((cm)^2*(ky)^-1)) | Water content (%) |
|---|---|---|---|---|---|---|---|---|---|---|---|---|---|---|---|---|
| 11 | 32,08 | 22,97 | 39,270 | 0,232 | 0,817 | 0,585 | 0,051 | 50,819 | 29,725 | 397,693 | 11822 | 13,714 | 408 | 1,04 | 31 | 28,398 |
| 21 | 23,32 | 14,54 | 39,270 | 0,224 | 0,594 | 0,370 | 0,051 | 50,819 | 18,816 | 247,593 | 4659 | 4,952 | 93 | 0,41 | 8 | 37,650 |
| 36 | 25,52 | 15,86 | 39,270 | 0,246 | 0,650 | 0,404 | 0,051 | 50,819 | 20,524 | 540,227 | 11088 | 15,889 | 326 | 1,39 | 29 | 37,853 |
| 51,5 | 29,31 | 20,06 | 39,270 | 0,236 | 0,746 | 0,511 | 0,051 | 50,819 | 25,960 | 1718,345 | 44607 | 134,596 | 3494 | 0,3 | 8 | 31,559 |
| 63 | 25,67 | 15,63 | 39,270 | 0,256 | 0,654 | 0,398 | 0,051 | 50,819 | 20,227 | 767,754 | 15529 | 42,226 | 854 | 0,03 | 1 | 39,112 |
| 75 | 22,89 | 13,08 | 39,270 | 0,250 | 0,583 | 0,333 | 0,051 | 50,819 | 16,927 | 691,514 | 11705 | 55,046 | 932 | 0 | 0 | 42,857 |
| 88 | 19,7 | 9,15 | 39,270 | 0,269 | 0,502 | 0,233 | 0,051 | 50,819 | 11,841 | 1337,705 | 15840 | 32,787 | 388 | 0 | 0 | 53,553 |
| 99 | 30,87 | 19,67 | 39,270 | 0,285 | 0,786 | 0,501 | 0,051 | 50,819 | 25,455 | 514,743 | 13103 | 52,618 | 1339 | 0,05 | 1 | 36,281 |
| 110 | 23,36 | 12,67 | 39,270 | 0,272 | 0,595 | 0,323 | 0,051 | 50,819 | 16,396 | 599,526 | 9830 | 19,890 | 326 | 0,24 | 4 | 45,762 |
| 120 | 22,75 | 13,43 | 39,270 | 0,237 | 0,579 | 0,342 | 0,051 | 50,819 | 17,380 | 338,421 | 5882 | 43,559 | 757 | 0,3 | 5 | 40,967 |
| 130 | 26,57 | 15,15 | 39,270 | 0,291 | 0,677 | 0,386 | 0,051 | 50,819 | 19,606 | 400,000 | 7842 | 27,723 | 544 | 0,13 | 3 | 42,981 |
| 140 | 24,52 | 14,17 | 39,270 | 0,264 | 0,624 | 0,361 | 0,051 | 50,819 | 18,337 | 399,234 | 7321 | 21,776 | 399 | 0,35 | 6 | 42,210 |
| 150 | 40,05 | 24,23 | 39,270 | 0,403 | 1,020 | 0,617 | 0,051 | 50,819 | 31,356 | 780,025 | 24458 | 59,430 | 1863 | 0,29 | 9 | 39,501 |
| 160 | 23,41 | 13,54 | 39,270 | 0,251 | 0,596 | 0,345 | 0,051 | 50,819 | 17,522 | 608,863 | 10669 | 15,953 | 280 | 0,15 | 3 | 42,161 |
| 170 | 23,3 | 13,07 | 39,270 | 0,261 | 0,593 | 0,333 | 0,051 | 50,819 | 16,914 | 377,008 | 6377 | 8,607 | 146 | 0,15 | 3 | 43,906 |
| 180 | 24,08 | 13,9 | 39,270 | 0,259 | 0,613 | 0,354 | 0,051 | 50,819 | 17,988 | 118,165 | 2126 | 3,237 | 58 | 0 | 0 | 42,276 |
| 191,5 | 34,53 | 21,07 | 39,270 | 0,343 | 0,879 | 0,537 | 0,121 | 120,773 | 64,800 | 398,102 | 25797 | 3,417 | 221 | 0,33 | 21 | 38,981 |
| 202 | 30,07 | 16,91 | 39,270 | 0,335 | 0,766 | 0,431 | 0,121 | 120,773 | 52,006 | 93,140 | 4844 | 1,140 | 59 | 0,18 | 9 | 43,765 |
| 210 | 21,83 | 12,74 | 39,270 | 0,231 | 0,556 | 0,324 | 0,121 | 120,773 | 39,181 | 288,226 | 11293 | 5,651 | 221 | 0,16 | 6 | 41,640 |
| 222 | 30,49 | 18,93 | 39,270 | 0,294 | 0,776 | 0,482 | 0,121 | 120,773 | 58,218 | 225,040 | 13101 | 4,226 | 246 | 0,53 | 31 | 37,914 |
| 234 | 24,67 | 13,86 | 39,270 | 0,275 | 0,628 | 0,353 | 0,121 | 120,773 | 42,626 | 242,031 | 10317 | 2,361 | 101 | 0 | 0 | 43,818 |
| 241 | 29,12 | 17,4 | 39,270 | 0,298 | 0,742 | 0,443 | 0,038 | 37,801 | 16,749 | 477,931 | 8005 | 6,207 | 104 | 0,69 | 12 | 40,247 |
| 250 | 35,14 | 21,92 | 39,270 | 0,337 | 0,895 | 0,558 | 0,038 | 37,801 | 21,100 | 254,562 | 5371 | 3,519 | 74 | 2,78 | 59 | 37,621 |
| 262 | 27,57 | 16,94 | 39,270 | 0,271 | 0,702 | 0,431 | 0,038 | 37,801 | 16,306 | 121,606 | 1983 | 1,181 | 19 | 3,13 | 51 | 38,556 |
| 265,6 | 32,13 | 19,61 | 39,270 | 0,319 | 0,818 | 0,499 | 0,038 | 37,801 | 18,876 | 186,334 | 3517 | 1,836 | 35 | 8,67 | 164 | 38,967 |
| 269,5 | 27,99 | 17,51 | 39,270 | 0,267 | 0,713 | 0,446 | 0,038 | 37,801 | 16,855 | 84,216 | 1419 | 1,186 | 20 | 0,57 | 10 | 37,442 |
| 287 | 30,77 | 20,11 | 39,270 | 0,271 | 0,784 | 0,512 | 0,038 | 37,801 | 19,358 | 290,261 | 5619 | 29,410 | 569 | 5,42 | 105 | 34,644 |
| 298 | 35,99 | 23,88 | 39,270 | 0,308 | 0,916 | 0,608 | 0,038 | 37,801 | 22,987 | 76,382 | 1756 | 2,680 | 62 | 41,08 | 944 | 33,648 |
| 310 | 31,38 | 21,01 | 39,270 | 0,264 | 0,799 | 0,535 | 0,038 | 37,801 | 20,224 | 211,328 | 4274 | 5,712 | 116 | 6,47 | 131 | 33,047 |
| 320 | 27,1 | 17,76 | 39,270 | 0,238 | 0,690 | 0,452 | 0,038 | 37,801 | 17,096 | 74,700 | 1277 | 1,877 | 32 | 1,86 | 32 | 34,465 |
| 330 | 27,52 | 18,33 | 39,270 | 0,234 | 0,701 | 0,467 | 0,038 | 37,801 | 17,644 | 92,471 | 1632 | 2,455 | 43 | 2,95 | 52 | 33,394 |
| 339 | 25,31 | 16,09 | 39,270 | 0,235 | 0,645 | 0,410 | 0,038 | 37,801 | 15,488 | 44,103 | 683 | 0,430 | 7 | 0,87 | 13 | 36,428 |
| 350 | 24,77 | 15,42 | 39,270 | 0,238 | 0,631 | 0,393 | 0,038 | 37,801 | 14,843 | 65,499 | 972 | 0,973 | 14 | 1,62 | 24 | 37,747 |
| 360 | 34,23 | 22,05 | 39,270 | 0,310 | 0,872 | 0,561 | 0,038 | 37,801 | 21,225 | 72,789 | 1545 | 1,361 | 29 | 1,36 | 29 | 35,583 |
| 370 | 30,49 | 19,45 | 39,270 | 0,281 | 0,776 | 0,495 | 0,038 | 37,801 | 18,722 | 53,026 | 993 | 0,500 | 9 | 3,44 | 64 | 36,209 |
| 380 | 31,25 | 18,76 | 39,270 | 0,318 | 0,796 | 0,478 | 0,038 | 37,801 | 18,058 | 32,383 | 585 | 0,400 | 7 | 0,75 | 14 | 39,968 |
| 388 | 28,51 | 18,92 | 39,270 | 0,244 | 0,726 | 0,482 | 0,038 | 37,801 | 18,212 | 44,850 | 817 | 10,646 | 194 | 2,11 | 38 | 33,637 |
| 403 | 25,08 | 15,65 | 39,270 | 0,240 | 0,639 | 0,399 | 0,038 | 37,801 | 15,064 | 98,243 | 1480 | 0,958 | 14 | 4,22 | 64 | 37,600 |
| 414 | 25,51 | 16,97 | 39,270 | 0,217 | 0,650 | 0,432 | 0,038 | 37,801 | 16,335 | 35,071 | 573 | 9,580 | 156 | 1,89 | 31 | 33,477 |
| 423 | 25,63 | 17,09 | 39,270 | 0,217 | 0,653 | 0,435 | 0,038 | 37,801 | 16,451 | 0,000 | 0 | 0,000 | 0 | 0 | 0 | 33,320 |
| 430 | 24,98 | 16,4 | 39,270 | 0,218 | 0,636 | 0,418 | 0,038 | 37,801 | 15,786 | 0,000 | 0 | 0,061 | 1 | 0,18 | 3 | 34,347 |
| 436 | 23,2 | 15,41 | 39,270 | 0,198 | 0,591 | 0,392 | 0,038 | 37,801 | 14,833 | 0,000 | 0 | 0,000 | 0 | 0 | 0 | 33,578 |
| 443,5 | 26,17 | 18,33 | 39,270 | 0,200 | 0,666 | 0,467 | 0,038 | 37,801 | 17,644 | 0,327 | 6 | 0,000 | 0 | 4,69 | 83 | 29,958 |
| 448 | 27,78 | 21,79 | 39,270 | 0,153 | 0,707 | 0,555 | 0,038 | 37,801 | 20,975 | 0,000 | 0 | 0,000 | 0 | 15,92 | 334 | 21,562 |
| 453 | 22,97 | 15,89 | 39,270 | 0,180 | 0,585 | 0,405 | 0,038 | 37,801 | 15,296 | 0,441 | 7 | 0,000 | 0 | 0,19 | 3 | 30,823 |

# References

Aagaard, K., and Greisman, P., 1975. Towards new mass and heat budgets in the Arctic Ocean, J. Geophys. Res., 80, 3821–3827.

Aagaard, K., Swift, J.H., Carmack, E.C., 1985. Thermohaline circulation in the Arctic Mediterranean Seas. J. Geophys. Res. 90, 4833–4846.

Andrews, J.T. and Tedesco, K., 1992. Detrital carbonate-rich sediments, northwest Labrador Sea: implications for ice-sheet dynamics and iceberg rafting Heinrich events in the North Atlantic. Geology 20, 1087e1090.

Armstrong, H. and Brasier, M., 2005. Microfossils. I: *Microfossils, second edition.* s.l.:s.n.

Barrientos, N., Lear, C.H., Jakobsson, M., Stranne, C., O'Regan, M., Cronin, T.M., Gukov, A.Y., Coxall, H.K., 2018. Arctic Ocean benthic foraminifera Mg/Ca ratios and global Mg/Ca-temperature calibrations: new constraints at low temperatures. Geochim. Cosmochim. Acta 236, 240–259.

Batchelor, C., Dowdeswell, J., and Hogan, K., 2011. Late Quaternary ice flow and sediment delivery through Hinlopen Trough, Northern Svalbard margin: submarine landforms and depositional fan. Marine Geology, 284(1), 13-27.

Beszczynska-Möller, A., Fahrbach, E., Schauer, U., Hansen, E., 2012. Variability in Atlantic water temperature and transport at the entrance of the Arctic Ocean 1997–2010. ICES Journal of Marine Science 69, 852–863. http://dx.doi.org/ 10.1093/icesjms/fss056.

Beszczynska-Möller, A., Woodgate, R.A., Lee, C., Melling, H., Karcher, M., 2011. A synthesis of exchanges through the main oceanic gateways to the Arctic Ocean. Oceanography 24, 82–99.

Bond, G. and Lotti, R., 1995. Iceberg discharges into the North Atlantic on millennial time scales during the last glaciation. Science 267, 1005–1010 (1995).

Chapman, W.L. and Walsh, J.E., 2007. Simulations of arctic temperature and pressure by global coupled models. J Climate, 20, 609-632.

Clark, C.D., 1993. Mega-scale glacial lineations and cross-cutting ice-flow landforms. Earth Surface Processes and Landforms 18, 1–29.

Dallmann, W., 2015. Geoscience atlas of Svalbard. Tromsø: Norsk Polarsinstitutt.

Dansgaard, W., 1985. Greenland ice core studies. Palaeogeography, Palaeoclimatology, Palaeoecology, 50 (1985): 185--187

Dansgaard, W., Johnsen, S.J, Clausen, H.B., Dahl-Jensen, D., Gundestrup, N.S., Hammer, C.U., Hvidberg, C.S., Steffensen, J.P., Sveinbjörnsdottir, A.E., Jouzel, J., Bond, G., 1993. Evidence for general instability of past climate from a 250-kyr ice-core record. Nature 364, 218–220 (1993).

Dowdeswell J.A., 2009. Ice-Rafted Debris (IRD). In: Gornitz V. (eds) Encyclopedia of Paleoclimatology and Ancient Environments. Encyclopedia of Earth Sciences Series. Springer, Dordrecht.

Espitalié, J., Laporte, J. L., Madec, M., Marquis, F., Leplat, P., Paulet, J. and Boutefeu, A., 1997. Méthode rapide de characterisation des roches-mere, de leur potential petrolier et de leur degre d'évolution, Revue de l'Institute Francais du Petrole, 32, 23–42.

Forwick, M., Vorren, T. O., Hald, M., Korsun, S., Roh, Y., Vogt, C., Yoo, K.C., 2010. Spatial and temporal influence of glaciers and rivers on the sedimentary environment in Sassenfjorden and Tempelfjorden, Spitsbergen, in Fjord Systems and Archives, vol. 344, edited by: Howe, J. A., Austin, W. E. N., Forwick, M., and Paetzel, M., 163–193, Geological Society, London.

Grousset, F.E., Labeyrie, L., Sinko, J.A., Cremer, M., Bond, G., Duprat, J., Cortijo, E., Huon, S., 1993. Patterns of ice-rafted detritus in the Glacial North Atlantic (40-55°N). Paleoceanography 8, 175-192.

Hald, I., 2017. Analyse av total karbon, total organisk karbon og total svovel. IG, Universitetet i Tromsø.

Hald, M. and Steinsund, P.I., 1996. Benthic foraminifera and carbonate dissolution in the surface sediments of the Barents and Kara Seas. Berichte Polarforschung 212, 285–307.

Hancock, J.M., 1984. Introduction to the Petroleum Geology of the North Sea (ed. Glennie, K.W.). 133-150, Blackwell, Oxford

Hebbeln, D., Dokken, T., Andersen, E., Hald, M., Elverhøi, A., 1994. Moisture supply for northern ice-sheet growth during the Last Glacial Maximum. *Nature*, 370(6488), pp.357-360.

Heinrich, H., 1988. Origin and consequences of cyclic ice rafting in the Northeast Atlantic Ocean during the past 130,000 years, Quat. Res., 29(2), 142–152.

Hopkins, T., 1991. The GIN Sea—A synthesis of its physical oceanography and literature review 1972–1985. *Earth-Science Reviews*, 30(3-4), pp.175-318.

Houghton, J., 2009. Global Warming. The Complete Briefing. Fourth Edition. Cambridge University Press, New York, United States of America.

Huber, R., Meggers, H., Baumann, K.H., Henrich, R., 2000. Recent and Pleistocene carbonate dissolution in sediments of the Norwegian-Greenland Sea, Mar. Geol., 165, 123–136.

Javaux, E.J. and Benzerara, K., 2009. Microfossils. CR. Palevol 8, 605-615.

Jessen, S.P., Rasmussen, T.L., Nielsen, T., Solheim, A., 2010. A new Late Weichselian and Holocene marine chronology for the western Svalbard slope 30,000 - 0 cal years BP. Quaternary Science Reviews 29, 1301-1312. doi: 10.1016/j.quascirev.2010.02.020

Jones, R.W., 1994. The Challenger foraminifera. Oxford University Press, Oxford

Kendall, M.A., 1996. Are Arctic soft sediment macrobenthic communities impoverished? Polar Biology 16, 393-399.

Kimoto, K., 2015. Planktonic foraminifera. In: Ohtsuka, S., Suzaki, T., Horiguchi, T, Suzuki, N., 2015. Marine Protists. Diversity and Dynamics. DOI 10.1007/978-4-431-55130-0. Springer, Japan

Kissel, C., Laj, C., Lehman, B., Labyrie, L., Bout-Roumazeilles, V., 1997. Changes in the strength of the Iceland-Scotland overflow water in the last 200,000 years: Evidence from magnetic anisotropy analysis of core SU90-33. Earth and Planetary Science Letters 152, 25-36.

Knudsen, K.L., Jiang, H., Jansen, E., Eiriksson, J., Heinemeier, J., Seidenkrantz, M.S., 2004. Environmental changes of North Iceland during the deglaciation and the Holocene: foraminifera, diatoms and stable isotopes. Marine Micropa- leontology 50, 273–305.

Koc, N., Klitgaard-Kristensen, D., Hasle, K., Forsberg, C.F., Solheim, A., 2002. Late glacial palaoceanography of Hinlopen Strait, northern Svalbard. Polar Research 21(2), 307-314.

Kristensen, D.K., Rasmussen, T.L., Koc, N., 2013. Paleoceanographic changes in the northern Barents Sea during the last 16,000 years - new constraints on the last deglaciation of the Svalbard-Barents Sea Ice Sheet. Boreas 42, 798-813

Kuijpers, A., Nielsen, T., Akhmetzhanov, A., de Haas, H., Kenyon, N.H., van Weering, T.C.E., 2001. Late Quaternary slope instability on the Faeroe margin: mass flow features and timing of events. Geo-Marine Letters 20, 149-159.

Lehman, S.J., Jones, G.A., Keigwin, L.D., Andersen, E.S., Butenkoi, G., Østmo, S-R., 1991. Initiation of Fennoscandian ice-sheet retreat during the last glaciation. Nature 349, 513-516

Lekens, W.A.H., Sejrup, H.P., Haflidason, H., Petersen, G.Ø., Hjelstuen, B., Knorr, G., 2005. Laminated sediments preceding Heinrich event 1 in the Northern North Sea and Southern Norwegian Sea: Origin, processes and regional linkage. Marine Geology 216, 27-50.

Liu, Z., Carlson, A.E., He, F., Brady, E.C., Otto-Bliesner, B.L., Briegleb, B.P., Wehrenberg, M., Clark, P.U., Wu, S., Cheng, J., Zhang, J., Noone, D., Zhu, J., 2018. Younger Dryas cooling and the Greenland climate response to $CO_2$. PNAS July 10, 2012 109 (28) 11101-11104; https://doi.org/10.1073/pnas.1202183109

Marshall, J. and Plumb, R. A., 2008. Atmosphere, Ocean, and Climate Dynamics. An Introductory Text. Elsevier Academic Press, London, UK, p. 259-260, 274, 282-283.

Migeon, S., Weber, O., Faugeres, J. & Saint-Paul, J., 1998. SCOPIX: A new X-ray imaging system for core analysis. *Geo-Marine Letters.*

Moros, M., Kuijpers, A., Snowball, I., Lassen, S., Bäckström, D., Gingele, F., McManus, J., 2002. Were glacial iceberg surges in the North Atlantic triggered by climatic warming? Marine Geology 192, 393-417.

Nielsen, T. and Rasmussen, T.L., 2018: Reconstruction of ice sheet retreat after the Last Glacial Maximum in Storfjorden, southern Svalbard. Marine Geology 402, 228–242.

Ottesen, D., Dowdeswell, J.A., Landvik, J.Y., Mienert, J., 2007. Dynamics of the Late Weichselian ice sheet on Svalbard inferred from high-resolution sea-floor morphology. Boreas 36, 286–306.

Overland J.E., 2009. The case for global warming in the Arctic. In: Nihoul J.C.J., Kostianoy A.G. (eds) Influence of Climate Change on the Changing Arctic and Sub-Arctic Conditions. NATO Science for Peace and Security Series C: Environmental Security. Springer, Dordrecht

Pearson, P.N, Wade, B.S., Huber, B.T., 2018. Taxonomy, biostratigraphy, and phylogeny of Oligocene and early Miocene Paragloborotalia and Parasubbotina. Cushman Foundation Special Publication No. 46 p. 429-458, 2018

Pfirman, S., & Milliman, J., 1987. Morphology, geology and oceanography of the Hinlopen Strait and Trough, Svalbard, Norway. *Polar Research*, *5*(3), 297-298. https://doi.org/10.3402/polar.v5i3.6893

Pirrung, M., Futterer, D., Grobe, J., Matthiessen, F., 2002. Magnetic susceptibility and ice-rafted debris in surface sediments of the Nordic Seas: implications for Isotope Stage 3 oscillations. Geo-Marine letters 22, 1-11.

Polyak, L., Mikhailov, V., 1996. Post-glacial environments of the southeastern Barents Sea: foraminiferal evidence. In: Andrews, J.T., Austin, W.E.N., Bergsten, H., Jennings, A.E. (Eds.), Late Quaternary Paleoceanography of the North Atlantic margins. Geological Society Special Publication No. 111, London, pp. 323–337.

Rasmussen, T.L. and Thomsen, E., 2013. Pink marine sediments reveal rapid ice melt and Arctic meltwater discharge during Dansgaard-Oeschger warmings.Nature Communications 4, 2849, published 22/11 2013, doi: 10.1038/ncomms3849

Rasmussen, T. and Thomsen, E., 2015. Palaeoceanographic development in Storfjorden, Svalbard, during the deglaciation and Holocene: evidence from benthic foraminiferal records. An international journey of Quaternary research.

Rasmussen, T.L., Thomsen, E., van Weering, T.C.E., 1998. Cyclic changes in sedimentation on the Faeroe Drift 53-9 kyr BP related to climate variations. In: Stoker, M., Evans, D., Cramp, R. (Eds.), Geological Processes on Continental Margins: Sedimentation, Mass-Wasting and Stability. Geological Society Special Publications, 129, 255-267.

Rasmussen, T.L., Thomsen, E., Slubowska, M.A., Jessen, S., Solheim, A., Koc, N., 2006. Paleoceanographic evolution of the SW Svalbard margin (76°N) since 20,000 $^{14}$C yr BP. Sciencedirect.

Rasmussen, T.L., Thomsen, E., Slubowska, M.A., Jessen, S., Solheim, A., Koç, N., 2007. Paleoceanographic evolution of the SW Svalbard margin (76°N) since 20,000 $^{14}$C yr BP. Quaternary Research 67, 100-114.

Robinson, S., Maslin, M., McCave, I., 1995. Magnetic susceptibility variations in Upper Pleistocene deep-sea sediments of the NE Atlantic: implications for ice rafting and paleocirculation at the Last Glacial Maximum. Paleoceanography 10, 221-250.

Robinson, S.G., Sahota, J.T.S., Oldfield, F., 2000. Early diagenesis in North Atlantic abyssal plain sediments characterized by rock-magnetic and geochemical indices. Marine Geology 163, 77-107.

Rudels, B., Friedrich, H.J, Quadfasel, D., 1999. The Arctic circumpolar boundary current, Deep Sea Res., Part 2, 46, 1023-1062

Rudels, B., Korhonen, M., Schauer, U., Pisarev, S., Rabe, B., Wisotzki, A., 2014. Circulation and transformation of Atlantic water in the Eurasian Basin and the contribution of the Fram Strait inflow branch to the Arctic Ocean heat budget. *Progress in Oceanography*, 132, pp.128-152.

Saloranta, T. M. and Haugan, P. M., 200. Interannual variability in the hydrography of Atlantic water northwest of Svalbard. Journal of Geophysical Research 106, 13931–13943.

Schiebel, R. and Hemleben, C., 2005. Modern planktic foraminifera. Paläontologische Zeitschrift.

Serreze, M. C. and Francis, J. A. 2006. The arctic amplification debate. Climate Change 76, 241–264.

Slubowska, M., Koç, N., Rasmussen, T.L., Klitgaard-Kristensen, D., 2005. Changes in the flow of Atlantic water into the Arctic Ocean since the last deglaciation: Evidence from the northern Svalbard continental margin, 80°N. Paleoceanography, 20, PA4014, doi:10.1029/2005PA001141

Slubowska-Woldengen, M., Rasmussen, T.L., Koç, N., Klitgaard-Kristensen, D., Hald, M., Jennings, A.E., 2008. Time-slice reconstructions of ocean circulation changes on the continental shelf in the Nordic and Barents Seas during the last 16,000 cal yr B.P. Quaternary Science Reviews 27 (2008), 1476-1492

Slubowska-Woldengen, M., Rasmussen, T.L., Koç, N., Klitgaard-Kristensen, D., Nilsen, F., Solheim, A., 2007. Advection of Atlantic Water to the western and northern Svalbard shelf since 17,500 cal yr BP. Quaternary Science Reviews 26 (2007), 463-478

Snelgrove, P.V.R. and Butman, C.A., 1994. Animal-sediment interactions: cause versus effect. Oceanography and Marine Biology: An Annual Review 32, 111-177.

Stokes, C.R. and Clark, C.D., 1999. Geomorphological criteria for identifying Pleistocene ice streams. Annals of Glaciology 28, 67–74.

Stoner, J.S., Channell, J.E.T., Hillaire-Marcell, C., 1996. The magnetic signature of rapidly deposited detrital layers from the deep Labrador Sea: relationship to North Atlantic Heinrich layers. Paleoceanography 11, 309e325.

Vanneste, M., Mienert, J., Bünz, S., 2006. The Hinlopen Slide: A giant, submarine slope failure on the northern Svalbard margin, Arctic Ocean. Science Direct.

Voelker, A.H.L., et al., 2002. Global distribution of centennial-scale records for Marine Isotope Stage (MIS) 3: a database. Quat. Sci. Rev. 21, 1185–1212 (2002).

Wentworth C.K., 1922. A scale of grade and class terms for clastic sediments. Journal of Geology, Vol. 30, pp. 377-392.

Winkelmann, D., Geissles, W., Schneider, J., Stein, R., 2008. Dynamics and timing of the Hinlopen/Yermak Mega-slide north of Spitsbergen, Arctic Ocean. Marine Geology 250, 34–50.

Wollenburg, J.E., Knies, J., Mackensen, A., 2004. High-resolution paleoproductivity fluctuations during the past 24 kyr as indicated by benthic foraminifera in the marginal Arctic Ocean. Palaeogeography, Palaeoclimatology, Palaeoecology 204, 209–238.

Zamelczyk, K., Rasmussen, T., Husum, K., Godtliebsen, F., Hald, M., 2014. Surface water conditions and calcium carbonate preservation in the Fram Strait during marine isotope stage 2, 28.8-15.4 kyr. Paleoceanography, 29(1), pp.1-12.

Zamelczyk, K., Rasmussen, T.L., Husum, K., Haflidason, H., Vernal, A., Ravna, E.K., Hald, M., Hillaire-Marcel, C., 2012. Paleoceanographic changes and calcium carbonate dissolution in the central Fram Strait dur- ing the last 20ka yr, Quat. Res., 78, 405–416, doi:10.1016/j.yqres.2012.07.006.

Zamelczyk, K., Rasmussen, T.L., Husum, K., Hald, M., 2013. Marine cal- cium carbonate preservation vs. climate change over the last two millennia in the Fram Strait: Implications for planktic foraminiferal paleostudies, Mar. Micropaleontol., 98, doi:10.1016/j.marmicro.2012.10.001.